Whole-brain estimates of directed connectivity for human connectomics

Frässle, Stefan ; Manjaly, Zina M ; Do, Cao T ; Kasper, Lars ; Pruessmann, Klaas P ; Stephan, Klaas E

Abstract: Connectomics is essential for understanding large-scale brain networks but requires that individual connection estimates are neurobiologically interpretable. In particular, a principle of brain organization is that reciprocal connections between cortical areas are functionally asymmetric. This is a challenge for fMRI-based connectomics in humans where only undirected functional connectivity estimates are routinely available. By contrast, whole-brain estimates of effective (directed) connectivity are computationally challenging, and emerging methods require empirical validation. Here, using a motor task at 7T, we demonstrate that a novel generative model can infer known connectivity features in a whole-brain network (>200 regions, >40,000 connections) highly efficiently. Furthermore, graph-theoretical analyses of directed connectivity estimates identify functional roles of motor areas more accurately than undirected functional connectivity estimates. These results, which can be achieved in an entirely unsupervised manner, demonstrate the feasibility of inferring directed connections in whole-brain networks and open new avenues for human connectomics.

DOI: https://doi.org/10.1016/j.neuroimage.2020.117491

NeuroImage 225 (2021) 117491

Contents lists available at ScienceDirect

NeuroImage

journal homepage: www.elsevier.com/locate/neuroimage

Whole-brain estimates of directed connectivity for human connectomics

Stefan Frässle[a,*], Zina M. Manjaly[b], Cao T. Do[a], Lars Kasper[a,c], Klaas P. Pruessmann[c], Klaas E. Stephan[a,d,e]

[a] Translational Neuromodeling Unit (TNU), Institute for Biomedical Engineering, University of Zurich & ETH Zurich, Wilfriedstrasse 6, 8032 Zurich, Switzerland
[b] Department of Neurology, Schulthess, 8008 Zurich, Switzerland & Department of Health Sciences and Technology, ETH Zurich, Zurich, Switzerland
[c] Institute for Biomedical Engineering, ETH Zurich & University of Zurich, 8092 Zurich, Switzerland
[d] Wellcome Centre for Human Neuroimaging, University College London, London WC1N 3BG, United Kingdom
[e] Max Planck Institute for Metabolism Research, Cologne, Germany

ARTICLE INFO

Keywords:
Regression dynamic causal modeling
rDCM
Generative model
Effective connectivity
Connectomics
Visuomotor network

ABSTRACT

Connectomics is essential for understanding large-scale brain networks but requires that individual connection estimates are neurobiologically interpretable. In particular, a principle of brain organization is that reciprocal connections between cortical areas are functionally asymmetric. This is a challenge for fMRI-based connectomics in humans where only undirected functional connectivity estimates are routinely available. By contrast, whole-brain estimates of effective (directed) connectivity are computationally challenging, and emerging methods require empirical validation.

Here, using a motor task at 7T, we demonstrate that a novel generative model can infer known connectivity features in a whole-brain network (>200 regions, >40,000 connections) highly efficiently. Furthermore, graph-theoretical analyses of directed connectivity estimates identify functional roles of motor areas more accurately than undirected functional connectivity estimates. These results, which can be achieved in an entirely unsupervised manner, demonstrate the feasibility of inferring directed connections in whole-brain networks and open new avenues for human connectomics.

1. Introduction

Understanding the human brain is a major scientific challenge of our time. Advances in analysis methods for data from non-invasive neuroimaging techniques have provided unprecedented opportunities for studying the human brain (Friston, 2009; Poldrack and Farah, 2015). In particular, system models tailored to functional magnetic resonance imaging (fMRI) data have enabled studying the living human brain as a dynamic system of interconnected neuronal populations (Park and Friston, 2013). This has fueled the emergence of whole-brain connectomics, a young discipline which is fundamentally important for understanding the organizational principles of the brain and plays a central role in network neuroscience (Bassett and Sporns, 2017).

Since the term "connectome" was originally introduced (Hagmann, 2005; Sporns et al., 2005), the field has grown rapidly and is now one of the most vibrant disciplines in neuroscience (Craddock et al., 2013). One of the goals of connectomics is a comprehensive map of neuronal connections, covering the entire nervous system. Seminal achievements include the specification of the complete neuronal wiring diagram in *C. elegans* (White et al., 1986) or the visual system of *Drosophila* (Takemura et al., 2013). In non-human primates and humans, particular emphasis has been placed on differences and individuality. For example, an important concept is that of "connectivity fingerprints" – a term originally introduced to refer to area-specific patterns of connectivity (Passingham et al., 2002) and more recently used to denote subject-specific connectivity patterns that determine inter-individual differences in brain function (Tavor et al., 2016) and behavior (Smith et al., 2015). Furthermore, connectomics has begun incorporating changes in connectivity with cognitive context or learning (Froudist-Walsh et al., 2018).

Connectomics is not only crucial for studying organizational principles in the healthy human brain, but also in disease. Aberrant functional integration has been observed in most psychiatric and neurological disorders (Baker et al., 2019; Buckholtz and Meyer-Lindenberg, 2012; Fornito et al., 2015; Stam, 2014). For example, psychiatric diseases like schizophrenia, depression, and autism have all been associated with pathological alterations across the functional connectome. For this reason, connectomes may serve as intermediate phenotypes situated between the domains of genetics/molecules and expressions of individual (pathological) behavior (Fornito et al., 2015).

* Corresponding author.
E-mail address: stefanf@biomed.ee.ethz.ch (S. Frässle).

https://doi.org/10.1016/j.neuroimage.2020.117491
Received 20 September 2020; Received in revised form 13 October 2020; Accepted 21 October 2020
Available online 24 October 2020

However, to render connectomics useful for understanding large-scale brain networks and alterations thereof, individual connection estimates have to be neurobiologically interpretable. A principle of brain organization are functional asymmetries of reciprocal connections – e.g., differences between ascending and descending connections in cortical hierarchies (Felleman and Van Essen, 1991; Zeki and Shipp, 1988) or asymmetries in interhemispheric interactions (Frässle et al., 2016; Gazzaniga, 2000; Stephan et al., 2007). This however represents a challenge for fMRI-based connectomics in humans: routine measures of connectivity are so far undirected; namely, structural and functional connectivity among network nodes at a mesoscopic or macroscopic level. In brief, structural connectivity refers to white-matter fiber tracts that can be measured using diffusion weighted imaging (DWI; Schaefer et al., 2000), whereas functional connectivity relates to statistical interdependencies between fMRI signals and is computed using simple correlation analyses or more sophisticated statistical techniques (for a comprehensive review, see Karahanoglu and Van De Ville, 2017).

Unfortunately, inferring directed estimates of functional interactions (i.e., effective connectivity) at the whole-brain level has proven challenging, mainly due to computational limitations. Various models of effective connectivity have been proposed over the last decade (Bielczyk et al., 2019; Valdes-Sosa et al., 2011). For instance, dynamic causal models (DCMs; Friston et al., 2003) and biophysical network models (BNMs; Deco et al., 2013; Jirsa et al., 2016) are two widely used approaches and have proven useful. However, these methods are limited in either the network size that can be considered (DCM) or the ability to identify individual connection strengths (BNM). While recent progress has been made in both domains (Gilson et al., 2017; Razi et al., 2017; Wang et al., 2019), computational efficiency and identifiability remain problematic and/or unknown for these models.

Beyond DCM and BNM, several other approaches that infer directed estimates of functional interactions from neuroimaging data have been proposed. These include Multivariate Granger Causality (MVGC; Goebel et al., 2003; Roebroeck et al., 2005; Seth, 2010), Mesoscale Individualized Neurodynamic (MINDy) modeling (Singh et al., 2020), correlation generalizations (Xu et al., 2017), Group Iterative Multiple Model Estimation (GIMME; Gates et al., 2014), Bayes net (directed acyclic graphical) models (Mumford and Ramsey, 2014; Ramsey et al., 2017; Sanchez-Romero et al., 2019), and non-Gaussian models (Sanchez-Romero et al., 2018). While promising, all of these approaches also have limitations (e.g., some operate directly at the level of observed fMRI data, not at an underlying neuronal level), and their practical utility has not always been systematically tested in application to fMRI data from real-world scenarios.

Beyond methodological assessments of methods using synthetic data with known ground truth (e.g., Frässle et al., 2018a; Sanchez-Romero et al., 2019; Smith et al., 2011), empirical validation studies are required that challenge any given candidate model to rediscover known sets of connections from whole-brain fMRI data. This paper presents such a validation study for regression dynamic causal modeling (rDCM; Frässle et al., 2018a, 2017). rDCM is a recently introduced generative model of fMRI data that enables connection-specific estimates of effective connectivity in whole-brain networks. This method is promising for several reasons: First, rDCM is computationally highly efficient and scales gracefully to large networks that comprise hundreds of nodes. More precisely, compute times of rDCM scale polynomially (as opposed to exponentially) with the number of regions. Second, the model can exploit structural connectivity information to constrain inference on directed functional interactions or, where no such information is available, infer optimally sparse representations of whole-brain networks. Hence, rDCM provides two alternative modes of operation to derive individual connectivity fingerprints at the whole-brain level. Third, rDCM allows to exploit knowledge about where and when experimental perturbations (e.g., sensory stimuli) affect network dynamics. This is important since known perturbations can greatly help constrain inference about directed influences within systems (Stephan et al., 2015).

In this paper, we illustrate the practical benefits of rDCM for whole-brain connectomics and network neuroscience in humans. For this, we use ultra-high field 7T fMRI data acquired under a deliberately simple paradigm (visually paced hand movements) in which relevant connections are well known and show clear hemispheric asymmetries. Lateralized processes are particularly useful for this purpose as they provide strong qualitative predictions (Frässle et al., 2016; Stephan et al., 2007) that concern both the location (hemisphere) where processes should occur (or, equally important, not occur) as well as the asymmetry (or mirror symmetry) of processes across hemispheres. Here, we demonstrate the utility of rDCM by performing two types of whole-brain connectivity analyses in a network with over 200 regions and 40,000 directed connections. These analyses are (i) anatomically guided by tractography results, and (ii) completely unconstrained by pruning fully (all-to-all) connected brain-wide graphs to those connections essential for explaining whole-brain activity.

2. Methods and materials

2.1. Regression dynamic causal modeling

2.1.1. Basic framework

Regression DCM (rDCM) is a novel variant of DCM for fMRI that has specifically been developed for effective connectivity analyses in large (whole-brain) networks (Frässle et al., 2017). For this, rDCM applies several modifications and simplifications to the original DCM framework (for a short summary of classical DCM, see Supplementary Material S1). In brief, these include (i) translating state and observation equations from time to frequency domain using the Fourier transformation (under stationarity assumptions), (ii) replacing the nonlinear biophysical model of hemodynamics with a linear hemodynamic response function (HRF), (iii) applying a mean field approximation across regions (i.e., connectivity parameters targeting different regions are assumed to be independent), and (iv) specifying conjugate priors on neuronal (i.e., connectivity and driving input) parameters and noise precision to enable analytic variational Bayesian (VB) update equations. These modifications essentially transform a linear DCM in the time domain into a Bayesian linear regression (Bishop, 2006) in the frequency domain:

$$p\left(Y|\theta,\tau,X\right) = \prod_{r=1}^{R} \mathcal{N}\left(Y_r; X\theta_r, \tau_r^{-1} I_{N\times N}\right)$$

$$Y_r = \left(e^{2\pi i \frac{m}{N}} - 1\right)\frac{\hat{y}_r}{T}$$

$$X = \left[\hat{y}_1, \hat{y}_2, \ldots, \hat{y}_R, \hat{h}\hat{u}_1, \hat{h}\hat{u}_2, \ldots, \hat{h}\hat{u}_K\right]$$

$$\theta_r = \left[a_{r,1}, a_{r,2}, \ldots, a_{r,R}, c_{r,1}, c_{r,2}, \ldots, c_{r,K}\right] \quad (1)$$

where Y_r is the Fourier transform of the temporal derivative of the BOLD signal in region r that is explained as a linear mixture of afferent connections from other regions and direct (driving) inputs, y_r is the measured BOLD signal in region r, X is the design matrix (comprising a set of regressors and explanatory variables), and u_k is the kth experimental input. Additionally, N represents the number of data points, T the time interval between subsequent points, $\boldsymbol{m} = [0, 1, \ldots, N-1]$ is a vector of frequency indices, and h denotes the fixed hemodynamic response function (HRF). Furthermore, θ_r represents the parameter vector comprising all connections $a_{r,1}, ..., a_{r,R}$ and all driving input parameters $c_{r,1}, \ldots, c_{r,K}$ targeting region r. Effective connectivity parameters in DCM represent rate constants and are given in Hz (for details, please see Supplementary Material S1). Finally, τ_r denotes the noise precision parameter for region r and $I_{N\times N}$ is the identity matrix (where N denotes the number of data points). Under this formulation, inference can be done very efficiently by (iteratively) executing a set of analytical VB update equations concerning the sufficient statistics of the posterior density. In addition,

one can derive an expression for the negative (variational) free energy (Friston et al., 2007). The negative free energy represents a lower-bound approximation to the log model evidence that accounts for both model accuracy and complexity. Hence, the negative free energy offers a sensible metric for scoring model goodness and thus serves as a criterion for comparing competing hypotheses (Bishop, 2006). A comprehensive description of the generative model underlying rDCM can be found elsewhere (Frässle et al., 2017).

2.1.2. Sparsity constraints

The standard rDCM framework has recently been augmented with sparsity constraints to enable automatic pruning of fully (all-to-all) connected networks to a degree of optimal sparsity (Frässle et al., 2018a). This is achieved by introducing an additional set of binary indicator variables as feature selectors in the likelihood function. In particular, each connectivity and driving input parameter i in a fully connected model is multiplied with a specific binary indicator variable ξ_i which takes the value of 1 if the connection is present (i.e., contributes to explaining the observed signal) and 0 if the connection is absent (i.e., not involved in generating the observed signal). The Bayesian sparse linear regression model in the frequency domain takes the form:

$$p(Y|\theta,\tau,X) = \prod_{r=1}^{R} \mathcal{N}\left(Y_r; XZ_r\theta_r, \tau_r^{-1} I_{N\times N}\right)$$

$$Y_r = \left(e^{2\pi i \frac{m}{N}} - 1\right)\frac{\hat{y}_r}{T}$$

$$X = \left[\hat{y}_1, \hat{y}_2, \ldots, \hat{y}_R, \hat{h}\hat{u}_1, \hat{h}\hat{u}_2, \ldots, \hat{h}\hat{u}_K\right]$$

$$\theta_r = \left[a_{r,1}, a_{r,2}, \ldots, a_{r,R}, c_{r,1}, c_{r,2}, \ldots, c_{r,K}\right]$$

$$Z_r = \mathrm{diag}\left(\left[\xi_{r,1}, \xi_{r,2}, \ldots, \xi_{r,R}, \xi_{r,R+1}, \xi_{r,R+2}, \ldots, \xi_{r,R+K}\right]\right) \quad (2)$$

Where Z_r is a diagonal matrix comprising the binary indicator variables ξ for all connections and driving inputs targeting region r. All other variables in Eq. (2) are defined as above. For this framework, one can again derive a VB update scheme for model inversion to obtain estimates of (i) the posterior distribution over neuronal connectivity, noise precision and binary indicator parameters, and (ii) the negative free energy. As in the basic rDCM framework, model inversion then boils down to iteratively solving a set of update equations. For a comprehensive description of the generative model, we refer the reader to previous work (Frässle et al., 2018a).

Notably, a Bernoulli prior is specified on the binary indicator variables ξ_i where the Bernoulli distribution is parameterized by a single parameter p_0^i. In other words, the p_0^i is a hyperparameter that determines the *a priori* belief about the network's degree of sparseness. When no strong prior knowledge is available regarding the sparseness of the network, a principled approach to determine the optimal p_0^i is to systematically vary p_0^i within a range of plausible values and select the hyperparameter with the highest negative free energy (Frässle et al., 2018a).

2.2. Empirical data

Here, we assess the utility of rDCM for inferring the effective connectivity pattern in a realistic whole-brain network based on empirical data from an fMRI study with a simple paradigm of visually paced hand movements. We chose this dataset for the following reasons: (i) the simple and robust nature of the task, (ii) the extensive knowledge available about the cortical network supporting hand movements (Ledberg et al., 2007; Rizzolatti and Luppino, 2001; Witt et al., 2008), (iii) the engagement of distributed cortical networks related to visual and motor aspects of the task, (iv) the high signal-to-noise ratio (SNR) of the data afforded by the 7 Tesla MR scanner on which the data was acquired,[1] and (v) the absence of modulatory influences,[2] which appeals to the linearity assumptions in rDCM. This allowed us to probe the plausibility of the whole-brain connectivity patterns inferred by rDCM.

2.2.1. Participants

Thirty right-handed individuals (14 females, 16 males; mean age: 59.2 ± 9.5 years, age range: 39–74 years) participated in this methodological study. Five participants had to be excluded from the analysis due to non-compliance with the task, missing data, or incorrect scanner settings, resulting in a final sample of 25 participants (13 females, 12 males; mean age: 58.2 ± 9.7 years, age range: 39–71 years). All were healthy with no history of psychiatric or neurological disease, brain pathology or abnormalities in brain morphology as indicated by their T1-weighted anatomical image. All participants were fluent German speakers. Half of the participants were regularly taking low-dose aspirin (100 mg per day). This is because the dataset used in this paper consists of two groups from a larger study that was purely observational (i.e., participants already took aspirin independently from our study). In the following, we treat participants with and without aspirin intake as one group, given that the present study is not interested in potential aspirin effects but merely serves to test the construct validity of rDCM for a simple paradigm. For completeness, we examined potentially confounding effects of aspirin on connectivity estimates and found that none of the whole-brain connectivity estimates presented below showed any significant differences between the two groups. For each participant, written informed consent was obtained prior to the experiment. The experimental protocol was in compliance with the Declaration of Helsinki and was performed with approval by the Cantonal Ethics Commission of Zurich (EK 09-2006 ETH).

2.2.2. Experimental procedure

The task used in this study was similar to the paradigm by Grefkes et al. (2008) in which participants had to perform visually synchronized whole-hand fist closings with either their left or right hand. Hand movements of different conditions (i.e., left or right) were separated into two scanning sessions (which deviates from the work by Grefkes and colleagues, where left- and right-hand movements were performed in alteration within a single session).

In each session, the experimental paradigm was a blocked design as follows: At the beginning of each block, an arrow was presented in the middle of the screen, indicating which hand to use in the upcoming block. The arrow then started blinking at a rate of 1.25 Hz for 16 s, dictating the rhythm of participants' hand movements (i.e., 20 fist closings per block). The stimulus onset time was 300 ms and the inter-stimulus interval was set to 500 ms. Subsequent blocks were interleaved with a resting period of the same length where participants did not perform hand movements but kept fixation in the center of the screen. Stimuli were presented using Cogent 2000 (v1.33; http://www.vislab.ucl.ac.uk/Cogent/index.html). Since each session comprised fist closings of only one condition, this dataset

[1] Early theoretical work demonstrated that the intrinsic SNR depends approximately linearly on the static magnetic field strength (Hoult and Lauterbur, 1979; Edelstein et al., 1986). In theory, the strength of the signal from an oscillating magnetization is proportional to the square of the magnetic field strength, whereas the strength of the noise scales (under certain assumptions) only linearly with the magnetic field strength. This theoretical prediction was later confirmed empirically, for instance, Vaughan et al. (2001) demonstrated an almost twofold increase in SNR at 7T as compared to 4T.

[2] More specifically, the present task only has a single experimental condition that can be adequately modeled using a linear model like rDCM. By contrast, experiments with multiple task conditions in a single experimental run require models like the original bilinear DCM (Friston et al., 2003) which allows for task-dependent perturbations of endogenous connectivity (A matrix) via modulatory influences (B matrix).

is particularly suitable for probing the current implementation of rDCM since no modulatory influences are required.

As mentioned before, the task was chosen because it affords clear hypotheses about the putative network supporting visually synchronized hand movements (Ledberg et al., 2007; Rizzolatti and Luppino, 2001; Witt et al., 2008). Specifically, simple unilateral hand movements (i) result from lateralized brain activity (Kim et al., 1993) and (ii) involve interactions between well-known brain regions. We briefly comment on these properties in more detail.

Lateralized processes are particularly useful to evaluate models of connectivity as they provide strong qualitative predictions (for previous examples, see Frässle et al., 2016; Stephan et al., 2007). These predictions concern the location (hemisphere) where processes should occur (or, equally important, not occur) as well as the asymmetry (or mirror symmetry) of processes across hemispheres. In our paradigm, unilateral hand movements should be accompanied by enhanced connectivity between motor areas in the contralateral hemisphere (Kraskov et al., 2011). Given the visual pacing input, one would also expect lateralized connectivity from visual (e.g., motion-sensitive area V5/MT) to motor areas via parietal areas (Ledberg et al., 2007; Rizzolatti and Luppino, 2001); the effect of lateralization may be less strong, however, since the visual input was presented centrally and thus did not specifically enter one hemisphere. In the motor domain, an additional advantage of our paradigm is that contrasting left and right unilateral hand movements allows for mirror-symmetric predictions: right-hand movements should lead to enhanced connectivity between left-hemispheric (but not the corresponding right-hemispheric) motor regions and vice versa. This offers an opportunity to test the replicability of our connectivity findings across hemispheres.

The key cortical components of the motor network underlying visually synchronized unilateral hand movements are well known (Grefkes et al., 2008; Witt et al., 2008). These include primary motor (M1) and somatosensory cortex (SM1), supplementary motor area (SMA), and lateral premotor cortex (PMC). In brief, M1 represents the main executive locus, with corticospinal projections which directly target lateral motor nuclei in the spinal cord (Evarts, 1981). PMC is involved in the execution of hand movements under sensory guidance (Goldberg, 1985), and was found to be crucial for transforming sensory information into appropriate motor behavior (Halsband and Passingham, 1982). SMA represents an integral component for planning and initiating voluntary hand movements (Grefkes et al., 2008; Rao et al., 1993). Furthermore, SM1 relates to somatosensory and proprioceptive aspects of motor acts (Penfield and Boldrey, 1937). In addition to the components mentioned above, the anterior cerebellum is involved in simple unilateral hand movements (Witt et al., 2008). Furthermore, given the visual pacing input, one would also expect visual areas such as the primary visual cortex and the motion-sensitive area V5/MT to be engaged.

2.2.3. Data acquisition

Functional images were acquired using a 7T MR scanner (Philips Achieva) with a 16-channel head matrix receiver coil. Images were obtained using a T_2*-weighted gradient echo-planar imaging (EPI) sequence (36 axial slices, TR = 2000 ms, TE = 25 ms, field of view (FoV) 220 × 220 × 108mm^3, voxel size 1.77 × 1.77 × 3 mm^3, flip angle 70°, SENSE factor 4) sensitive to the blood oxygen level dependent (BOLD) signal. Images covered the entire brain. In each session, 230 functional images were acquired, representing either brain activity during left- or right-hand fist closings. For each participant, an additional high-resolution anatomical image was acquired using a T1-weighted inversion-recovery turbo field echo (3D IR-TFE) sequence (150 slices, TR = 7.7 ms, TE = 3.5 ms, volume TR=4000 ms, inversion time 1200 ms, field of view (FoV) 240 × 240 × 135 mm^3, voxel size 0.9 × 0.9 × 0.9mm^3, flip angle 7°, SENSE factor 2 in phase and 1.5 in slice direction).

In addition to the MRI data, physiological recordings related to heart beats and breathing were recorded during scanning with a 4-electrode electrocardiogram (ECG) and a breathing belt, respectively.

2.2.4. Data processing and analysis

Functional images were analyzed using SPM12 (Statistical Parametric Mapping, version R6553, Wellcome Trust Centre for Neuroimaging, London, UK, http://www.fil.ion.ucl.ac.uk) and Matlab R2015a (Mathworks, Natick, MA, USA). Individual images were realigned to the mean image, unwarped, coregistered to the participant's high-resolution anatomical image, and normalized to the Montreal Neurological Institute (MNI) standard space using the unified segmentation-normalization approach. During spatial normalization, functional images were resampled to a voxel size of 2 × 2 × 2 mm^3. Finally, normalized functional images were spatially smoothed using an 8 mm FWHM Gaussian kernel.

Model-based physiological noise correction based on peripheral recordings of cardiac (heart beat) and respiratory (breathing) cycles was performed using the PhysIO toolbox (Kasper et al., 2017). Specifically, the periodic effects of pulsatile motion and field fluctuations were modeled using Fourier expansions (i.e., sine and cosine basis functions) of different order for the estimated phases (RETROICOR) of cardiac pulsation (3rd order), respiration (4th order) and cardio-respiratory interactions (1st order). This resulted in 18 physiological noise regressors. The PhysIO toolbox is available as open source code as part of the TAPAS software suite (www.translationalneuromodeling.org/software).

Preprocessed functional images of every participant entered first-level General Linear Model analyses (GLM) to identify brain activity related to the experimental manipulation. The GLM comprised one task regressor, representing the periods when participants performed visually paced fist closings. The regressor was convolved with SPM's standard canonical hemodynamic response function. Additionally, we included the temporal and dispersion derivative of the canonical HRF ("informed basis set"; Friston et al., 1998). To control for movement-related and physiological artefacts, respectively, motion parameters (obtained from rigid-body realignment of the functional volumes) and physiological measures (obtained from physiological noise modeling in PhysIO) were included as nuisance regressors in the GLM. Finally, a high-pass filter was applied to remove low-frequency fluctuations (e.g., scanner drifts) from the data (cut-off frequency: 1/128 Hz).

Brain activity related to visually paced unilateral hand movements was then identified from the respective baseline contrasts of left- or right-hand movements. The individual contrast images were entered into random effects group level analyses (one-sample *t*-tests) for left- and right-hand fist closings, separately. Group-level BOLD activity was thresholded at $p < 0.05$, family-wise error (FWE)-corrected at the peak level.

2.2.5. Time series extraction

We used the Human Brainnetome atlas (Fan et al., 2016) as a whole-brain parcellation scheme to define regions of interest for subsequent effective connectivity analyses. The Brainnetome atlas represents a connectivity-based parcellation derived from non-invasive structural neuroimaging data obtained from DWI (http://atlas.brainnetome.org). The atlas comprises 246 distinct parcels (123 per hemisphere), including 210 cortical and 36 subcortical regions. We chose the Brainnetome atlas as a parcellation scheme for the following reasons: (i) the atlas is sufficiently fine-grained to allow for meaningful effective connectivity analyses at the whole-brain level, (ii) provides robust parcels across the population as demonstrated using cross-validation, and (iii) includes not only a parcellation of the human brain but also information on the structural connectivity among the 246 brain regions. In a first analysis, we used this structural information to inform the architecture of our network – that is, the endogenous connectivity matrix. Notably, the Brainnetome atlas (like most other state-of-the-art parcellation schemes) focusses on the cortex and does not cover the cerebellum. Hence, in the present study, we made the deliberate choice to focus on the cortex in

order to capitalize on the advantages of the Brainnetome atlas outlined above.

Due to signal dropouts in the raw functional images (especially in the parahippocampal gyrus and inferior temporal regions near the skull base), BOLD signal time series could not be extracted for all regions defined by the Brainnetome atlas. In summary, 215 regions could be extracted in all participants for both hand movement conditions. We further restricted this set to ensure interhemispheric consistency of the network – that is, if a region was present in one hemisphere but not the other, both parcels were discarded from further analysis (for a complete list of included and excluded regions, see Supplementary Table S1). This yielded a total of 208 brain regions from which sensible BOLD signal time series could be obtained in every participant (for a visualization of the individual mean coordinates of each parcel, see Supplementary Figure S1).

It is worth highlighting that a number of regions had to be excluded due to signal dropouts. This is likely due to several reasons: First, the data were not acquired with accelerated fMRI methods, such as inverse imaging or multiband techniques (Feinberg and Setsompop, 2013; Lin et al., 2012; Xu et al., 2013). Hence, in order to achieve a short TR, as is beneficial for effective connectivity analyses, relatively thick slices (3 mm) were acquired, exacerbating susceptibility-related dropouts in orbitofrontal and inferior temporal cortex. Second, susceptibility-related dropouts in the aforementioned regions are known to be more pronounced at ultra-high (7T) main field strengths (Balchandani and Naidich, 2015). Third, the required 3rd-order shim procedure to reduce field inhomogeneities is sensitive to head motion between pre-scans and functional runs. Finally, slice orientation (about −15 deg RL axis) and phase encoding blip direction (anterior to posterior) were not optimized to reduce dropouts in those regions. Having said this, we verified that none of the excluded regions represented a key component of the cerebral network supporting visually paced hand movements (Ledberg et al., 2007; Rizzolatti and Luppino, 2001; Witt et al., 2008).

Time series were then extracted as the principal eigenvariate of all voxels within a parcel. Time series were mean-centered and corrected for variance related to head movement, physiological noise, and derivatives of the hemodynamic response with regard to time and dispersion (Friston et al., 1998). The latter served to address a limitation of the current rDCM implementation which employs a fixed hemodynamic response function and therefore does not capture hemodynamic variability across brain regions and individuals (see Discussion). Extracted BOLD signal time series then entered effective connectivity analysis using rDCM.

2.2.6. rDCM analysis

For the rDCM analysis, we first used the structural connectome provided by the DWI data of the Brainnetome atlas to inform the connectivity architecture (i.e., the presence or absence of connections among brain regions in the A matrix) of the network (model 1; Fig. 1A). As DWI data contains no information on the directionality of fibers, connected nodes were always coupled by reciprocal connections. Additionally, the driving input (representing visually synchronized left- or right-hand fist closing movements) was allowed to elicit activity in all regions. This yielded a total of 16,868 free parameters (including 16,452 connectivity parameters, 208 inhibitory self-connections and 208 driving input parameters) to be estimated. To test the benefit of informing effective connectivity analyses by tractography-based measures, we further constructed two alternative networks: (i) a randomly permuted version of the Brainnetome structural connectome, discarding any regional specificity of connections while leaving the overall density of the network unchanged (model 2; Fig. 1B), and (ii) a fully (all-to-all) connected network where all 208 brain regions are linked via reciprocal connections (model 3; Fig. 1C).

In a second step, we tested whether rDCM also yielded sensible results in the absence of any *a priori* restrictions on model architecture by utilizing the embedded sparsity constraints of the method to automatically prune both connections and driving inputs. To this end, we assumed a fully connected network, where all 208 brain regions were coupled to each other via reciprocal connections. Additionally, the driving input was again allowed to elicit activity in all regions. This yielded a total of 43,472 free parameters to be estimated (including 43,056 connectivity parameters, 208 inhibitory self-connections and 208 driving input parameters). Starting from this fully connected network, model inversion then automatically pruned connection and driving input parameters to yield a sparse whole-brain effective connectivity pattern. Since exact *a priori* knowledge about the degree of sparseness of the network was not available, we followed the procedure described in Frässle et al. (2018a) to determine the optimal p_0^i. More specifically, for each participant, we systematically varied p_0^i within a range of 0.4 to 0.95 in steps of 0.05 and performed model inversion for each p_0^i value. The optimal p_0^i value was then determined for each participant by selecting the model that yielded the highest negative free energy. Note that we did not test smaller values of p_0^i for two reasons: (i) Due to the multimodal nature of the task (engaging motor, visual, somatosensory, proprioceptive, and top-down control regions) and the widespread BOLD activation pattern observed, a substantial degree of connectedness in the network was expected, and (ii) the structural connectome utilized in the previous anatomically informed analysis suggests a network density of approximately 0.4, which was used as the lower bound of our p_0^i-range.

2.2.7. Graph-theoretical analyses

Based on the inferred effective connectivity patterns underlying unilateral hand movements, we applied graph-theoretical measures (Bullmore and Sporns, 2009) to corroborate the pivotal role of motor regions in the pre- and postcentral gyrus during our task, as well as the known hemispheric lateralization of the network. We thus computed graph-theoretical measures that capture the relevance of each node and that have frequently been used in the field of connectomics: "betweenness centrality" and "node strength (in & out)". Betweenness centrality is defined as the fraction of all shortest paths in the network that contain a given node (Brandes, 2001; Freeman, 1977) and is given by the following expression:

$$C_B(i) = \frac{1}{(N-1)(N-2)} \sum_{h \neq i, h \neq j, i \neq j} \frac{\rho_{hj}(i)}{\rho_{hj}} \tag{3}$$

where $\rho_{hj}(i)$ is the number of shortest paths between h and j that pass through node i, ρ_{hj} is the number of all shortest paths between h and j, N is the number of nodes in the graph, and $(N-1)(N-2)$ is the number of node pairs that do not include node i.

Node strength (in & out) refers to the sum of weights of all afferent (incoming) and efferent (outgoing) links connected to a node and is computed using the following expression:

$$s_{in\ \&\ out}(i) = \sum_{i \neq j} w_{ij} + \sum_{i \neq j} w_{ji} \tag{4}$$

where w_{ij} is the weight of the connection from j to i. The first term captures the sum of all afferent (incoming) connections and the second term captures the sum of all efferent (outgoing) connections of node i.

Both graph-theoretical measures were computed using the implementations in the Brain Connectivity toolbox (Rubinov and Sporns, 2010).

3. Results

3.1. BOLD activity during unilateral hand movements

Brain activity related to visually synchronized whole-hand fist closings was assessed using random effects group analyses (one-sample *t*-tests). Consistent with previous findings, we observed significant activation in a widespread cortical network during left- and right-hand movements (Fig. 2; Supplementary Table S2), mainly lateralized to the

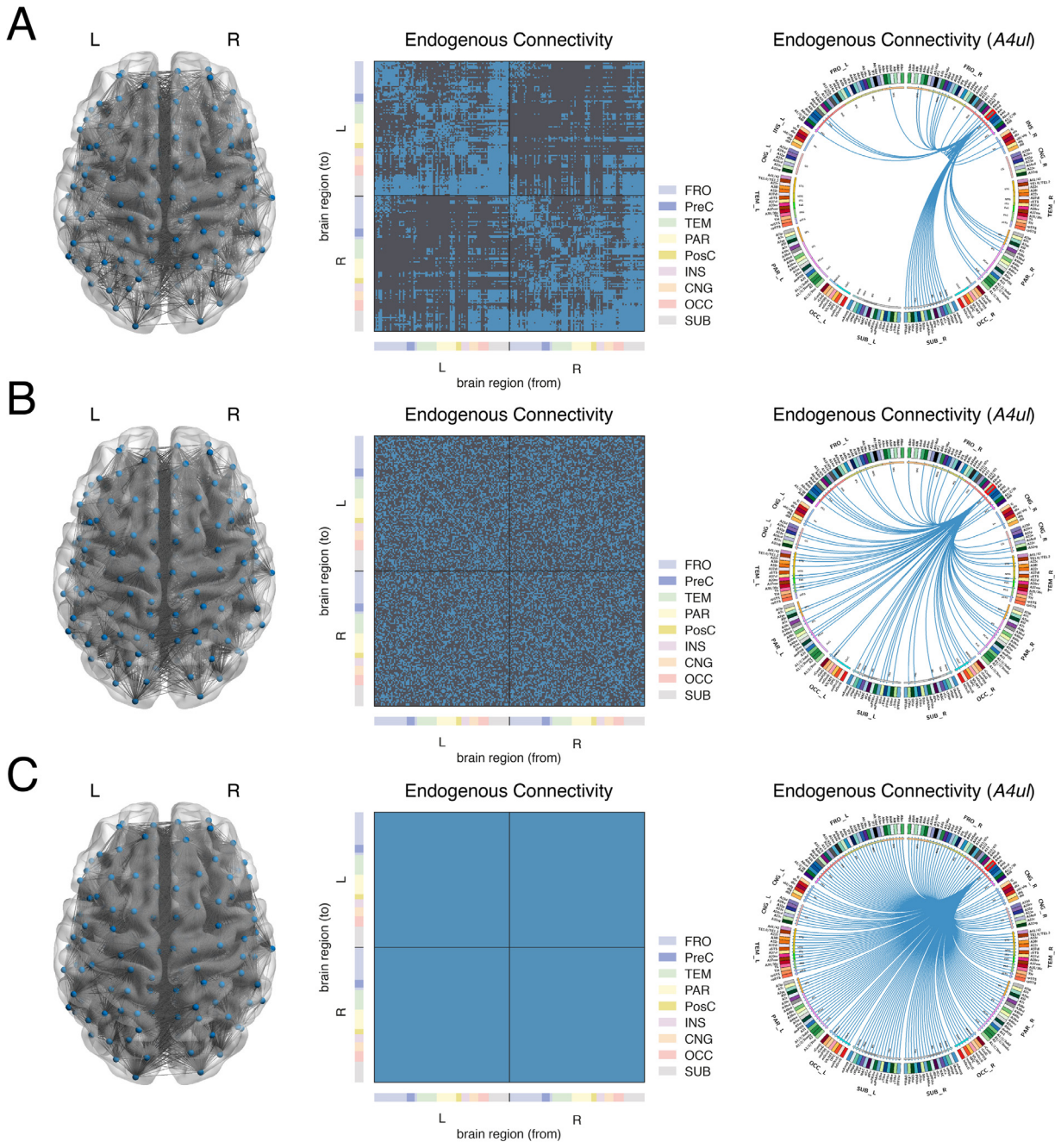

Fig. 1. Connectivity architecture of the whole-brain networks used to model effective connectivity during unilateral hand movements. The alternative models encode a network architecture that **(A)** was informed by the structural connectome provided by the Human Brainnetome atlas (model 1), **(B)** was a randomly permuted version of the Brainnetome structural connectome; thus, discarding any regional specificity of connections while leaving the overall density of the network unchanged (model 2), or **(C)** was a fully (all-to-all) connected network, where all regions were reciprocally connected (model 3). For each of the three models, the network architecture of the DCM is graphically projected onto a whole-brain volume (*left*) and shown as an adjacency matrix (*middle*). Regions are separated in left hemisphere (L) and right hemisphere (R). For each hemisphere, regions are divided into different sets, including frontal (FRO; *blue*), temporal (TEM; *green*), parietal (PAR; *yellow*), insular (INS; *purple*), cingulate[3] (CNG; *orange*), occipital (OCC; *red*), and subcortical (SUB; *grey*); as specified by the Brainnetome atlas. Additionally, we have explicitly highlighted regions of the precentral gyrus (PreC; *dark blue*) in the frontal lobe, as well as regions of the postcentral gyrus (PosC; *dark yellow*) in the parietal lobe as these are key components of the motor network. Finally, we also show exemplarily the sub-regional connectogram for the primary motor cortex (M1) in the precentral gyrus (Brainnetome parcel name: *A4ul*) (*right*). The labels on the outermost ring of the connectogram show again the anatomical set for each of the nodes: frontal, insula, cingulate, temporal, parietal, occipital, and subcortical. For each brain region defined by the Brainnetome atlas, an abbreviation and color are defined. Inside the parcellation ring, we show the outgoing connections from M1 in blue. The whole-brain volume representation was created using the BrainNet Viewer (Xia et al., 2013), which is freely available (http://www.nitrc.org/projects/bnv/). The connectogram was created using Circos, which is also publicly available (http://www.circos.ca/software/). *L* = left hemisphere; *R* = right hemisphere.

[3] In the Brainnetome nomenclature, this set of regions is called "LIM" (limbic). However, as the term "limbic" is not well-defined (Kötter & Stephan, 1997) and since "LIM" exclusively consists of cingulate areas, we prefer to call this set of regions "CNG" (cingulate).

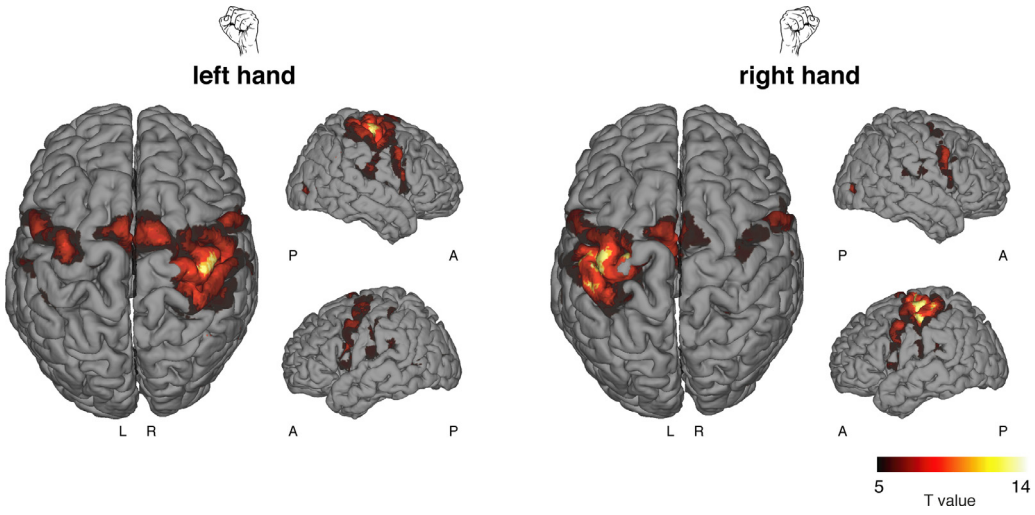

Fig. 2. BOLD activation during visually synchronized unilateral hand movements at the group level ($N = 25$). Left-hand (*left*) and right-hand fist closings (*right*) elicited activation in a distributed network, mainly lateralized to the contralateral hemisphere. Results are significant at a voxel-level threshold of $p < 0.05$ (family-wise error (FWE)-corrected). Results were rendered onto the surface of an anatomical template volume. L = left hemisphere; R = right hemisphere; A = anterior; P = posterior.

contralateral hemisphere. In particular, BOLD activation was located in the primary motor cortex (M1), premotor cortex (PMC), supplementary motor area (SMA), and the motion-sensitive area V5/MT in the extrastriate cortex ($p < 0.05$, FWE-corrected at peak level). Additionally, we observed BOLD activation in the ipsilateral cerebellum. As mentioned before, for the subsequent effective connectivity analyses, we utilized the Brainnetome atlas (Fan et al., 2016) as a whole-brain parcellation scheme which focuses on the cortex and does not cover the cerebellum.

3.2. *Regression DCM constrained by anatomical connectivity*

3.2.1. *Whole-brain effective connectivity during hand movements*

Individual connectivity parameters were estimated using rDCM where, in a first step, the network architecture of the DCMs was informed by the structural connectome from the Brainnetome atlas (model 1; Fig. 1A). Model inversion resulted in biologically plausible connectivity (Fig. 3B, left) and driving input patterns (Fig. 3B, right), suggesting pronounced functional integration in a widespread cortical network during visually paced unilateral hand movements. Consistent with our hypotheses (see Methods), rDCM revealed pronounced clusters of excitatory connections among motor and visual regions. Specifically, strong connections were observed among motor regions in the precentral (Brainnetome parcel name: *A4ul*) and postcentral gyrus (*A1/2/3ulhf, A2*), as well as the dorsal PMC (*A6cdl*) and the dorsal part of area 4 (*A4t*). Similarly, prominent functional integration was observed for the SMA (*A6m*) located in the superior frontal gyrus, as well as regions in the lateral occipital cortex, including the middle occipital gyrus (*mOccG*) and the motion-sensitive area (*V5/MT*). We also observed pronounced connections among regions in the parietal lobe (e.g., *A7c, A7m, A5m*), as well as excitatory connections from the parietal cortex to the visuomotor network highlighted above. Finally, connectivity was observed among frontal regions (e.g., *A8m, A6cvl, A44v*), as well as between frontal regions and all other components mentioned above. Overall, the majority of connections had positive weights (i.e., excitatory effects), which is consistent with the fact that our model describes changes of activity from baseline (i.e., activity induced by hand movements compared to rest). More precisely, positive weights are consistent with the fact that the GLM analyses revealed exclusively positive BOLD activations by our task (i.e., hand movements > rest) and no significant deactivations (i.e., rest > hand movements) when correcting for multiple comparisons. Furthermore, functional integration was strongest within hemispheres; however, pronounced interhemispheric connections were also observed, mainly among homotopic regions.

With regard to driving inputs (representing visually synchronized hand movements), we observed strong excitatory inputs to the motor and visual regions mentioned above (Fig. 3B, right). Driving inputs to motor-related regions were stronger for nodes in the contralateral as compared to the ipsilateral hemisphere.

Notably, the directedness of connectivity estimates obtained by rDCM is demonstrated by the fact that, for the present dataset, there are asymmetries between the afferent (incoming) and efferent (outgoing) parts of reciprocal connections. To provide an intuition of the degree of directedness in the connectivity estimates, it is instructive to inspect the degree of asymmetry in relation to the magnitude of the connection strengths themselves. This is because the degree of asymmetry can be maximally twice the magnitude of the strongest (in absolute terms) connection. On the contrary, the degree of asymmetry can be much smaller in scenarios where connections are strong; yet, differences between afferent and efferent parts are negligible. Here, we observed that differences in the strengths of afferent and efferent connections were comparable in magnitude with the connection strengths themselves (Fig. 3C). This suggested that rDCM goes beyond undirected measures like functional connectivity and can infer directedness in the connectivity patterns.

3.2.2. *Mirror symmetry of left- and right-hand movements*

Next, we investigated the effect of the hand movement condition (i.e., left vs. right hand) by testing, for each parameter, whether there was a significant difference between left- and right-hand fist closings (two-sided paired *t*-test). We found the expected mirror-symmetric pattern, with connections in the left hemisphere being increased during right-hand movements and, vice versa, connections in the right hemisphere being increased during left-hand movements (Fig. 4). These effects were highly specific in that only connections among sensorimotor areas showed significant hemispheric differences ($p < 0.05$, false discovery rate (FDR)-corrected for multiple comparisons across the 16,868 free parameters). Specifically, as expected for the task we used, we found increased intrahemispheric connectivity among regions in the contralateral precentral (M1 (*A4ul*), dorsal PMC (*A6cdl*)) and postcentral gyrus (SM1 (*A1/2/3ulhf, A2*)). Furthermore, intrahemispheric connectivity was increased among the contralateral SMA (*A6m*) and M1 and SM1.

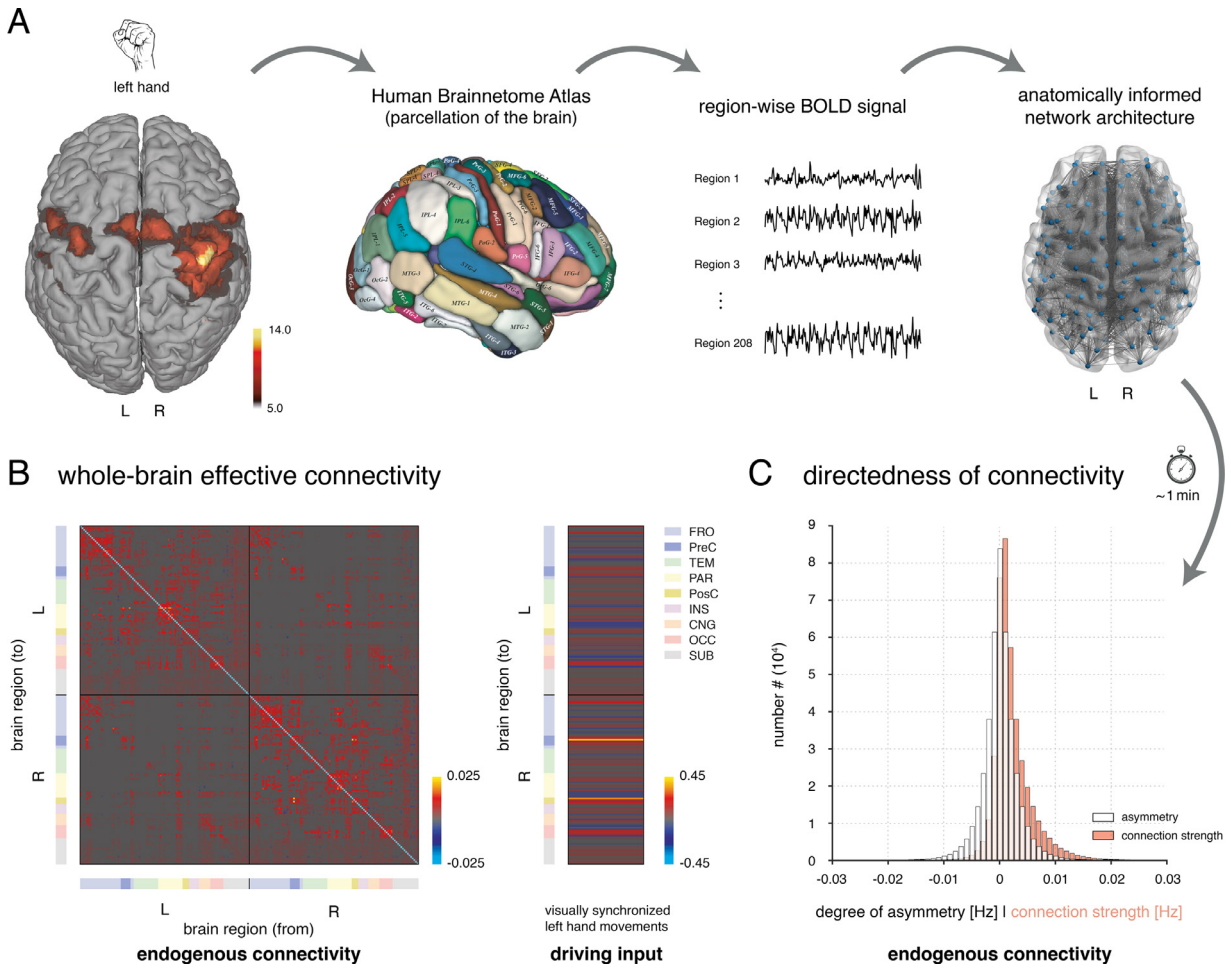

Fig. 3. Whole-brain effective connectivity pattern underlying unilateral hand movements as assessed with rDCM when using structural connectivity to inform the network architecture. **(A)** For the given BOLD activation pattern during visually synchronized hand movements, the Human Brainnetome atlas (Fan et al., 2016) was used as a whole-brain parcellation scheme. Region-wise BOLD signal time series were extracted for each participant individually as the principal eigenvariate and entered effective connectivity analyses using rDCM. **(B)** Mean posterior parameter estimates for connections (*left*) and driving inputs (*right*) during left-hand movements, averaged across participants. Regions are separated in left hemisphere (L) and right hemisphere (R). For each hemisphere, regions are divided into different sets, including frontal (FRO; *blue*), temporal (TEM; *green*), parietal (PAR; *yellow*), insular (INS; *purple*), cingulate (CNG; *orange*), occipital (OCC; *red*), and subcortical (SUB; *grey*); as specified by the Brainnetome atlas. Additionally, we have explicitly highlighted regions of the precentral gyrus (PreC; *dark blue*) in the frontal lobe, as well as regions of the postcentral gyrus (PosC; *dark yellow*) in the parietal lobe as these are key components of the motor network. The colormap is scaled with respect to the strongest between-region connection. **(C)** Histogram of asymmetry between the afferent (incoming) and efferent (outgoing) part of reciprocal connections (*white*). This suggests that the asymmetry was comparable in magnitude with the connection strengths themselves (*red*). Note that connectivity and driving input parameters represent rate constants and are thus given in Hz.

Finally, rDCM revealed increased interhemispheric connections among SMA and M1 and SM1 (although this was not significant for the connections between right SMA and left pre- and postcentral gyrus when correcting for multiple comparisons).

3.2.3. Benefit of informing network architecture with structural information

One might wonder whether utilizing the structural connectome from the Brainnetome atlas (Fan et al., 2016) to inform the network architecture of the whole-brain DCMs was beneficial for explaining the observed fMRI data. To this end, we constructed two alternative networks: Model 2 (Fig. 1B) represents a randomly permuted version of the Brainnetome structural connectome, and model 3 (Fig. 1C) assumes a fully (all-to-all) connected network where all regions are linked via reciprocal connections. Since functional integration in the brain is constrained (but not fully determined) by anatomical connections (Bullmore and Sporns, 2009; Passingham et al., 2002), one would expect that effective connectivity analyses benefit from including tractography-based measures.

We used random effects Bayesian model selection (BMS; Stephan et al., 2009b) to compare the competing whole-brain models based on their log model evidence (approximated by the negative free energy). We found decisive evidence that the anatomically informed model 1 was the winning model with a protected exceedance probability of 1. This illustrates clearly that models of whole-brain effective connectivity profit from structural connectivity measures derived from probabilistic tractography of DWI data. This is consistent with previous work in conventional (small-scale) DCMs that highlight the benefit of anatomically informed priors (Sokolov et al., 2019; Stephan et al., 2009c). To avoid any misunderstanding, it is worth remembering that Bayesian model selection only assesses the relative evidence for competing hypotheses (models) within a pre-specified model space and therefore our results do not imply that model 1 represents the "true" anatomical connectivity among the regions considered. Instead, our results simply demonstrate the benefit of using structural connectome information over a random or fully connected network architecture for explaining the measured fMRI data.

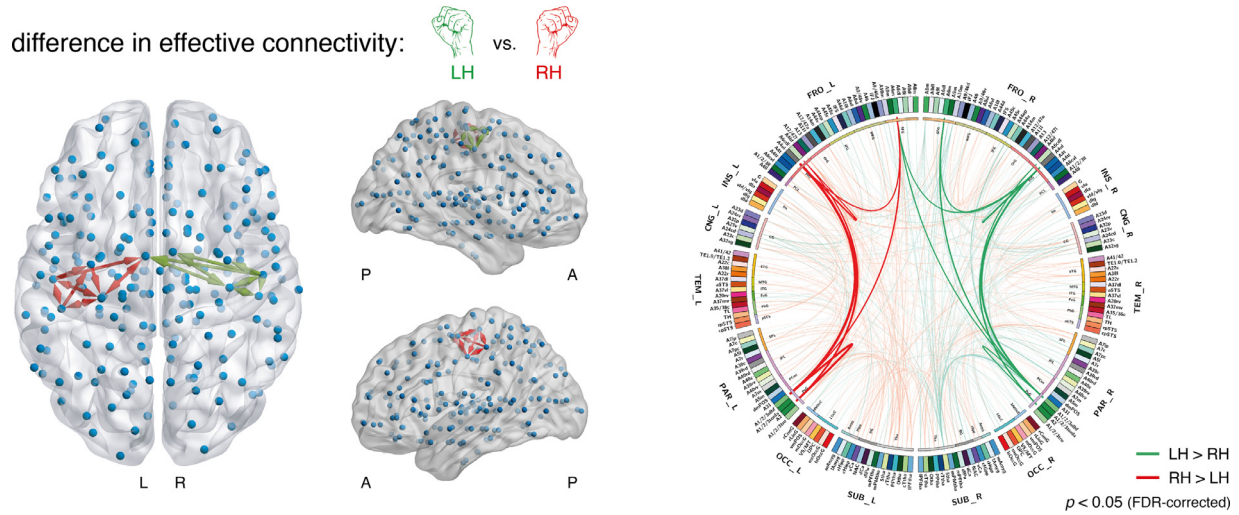

Fig. 4. Mirror symmetry of the effect of hand movement condition (i.e., left vs. right hand) in the motor network as assessed with rDCM when using an anatomically informed (fixed) network architecture. The differential effect of hand movement condition was graphically projected onto a whole-brain volume (*left*). Green arrows indicate connections that were significantly increased during left-hand movements as compared to right-hand movements; red arrows indicate connections that were significantly increased during right-hand movements compared to left-hand movements ($p < 0.05$, FDR-corrected for multiple comparisons). Note that edges in this graphical representation are directed. *L* = left hemisphere; *R* = right hemisphere; *A* = anterior; *P* = posterior. Results can also be inspected when graphically rendered as a connectogram (*right*). Solid lines represent the connections that showed a significant effect of the hand movement condition ($p < 0.05$, FDR-corrected). Lines with faded colors represent the subsequent 500 connections with the strongest differential effect (highest absolute T values of the two-sided paired *t*-test). The labels on the outermost ring show the anatomical lobe for each of the nodes: frontal, insula, cingulate, temporal, parietal, occipital, and subcortical. For each brain region defined by the Brainnetome atlas, an abbreviation and color are defined. Inside the parcellation ring, connections showing a significant effect of the hand movement condition are displayed as edges, with the color code defined as above (i.e., green = LH>RH, red = RH>LH).

3.3. *Regression DCM with sparsity constraints*

3.3.1. *Whole-brain effective connectivity during hand movements*

Next, we asked whether sensible whole-brain effective connectivity patterns could also be obtained in the absence of any *a priori* assumptions about the network's architecture. For this, rDCM with embedded sparsity constraints was used to prune, for each participant individually, a fully connected model containing over 43,000 free connectivity parameters (Fig. 5A).

Model inversion resulted in sparse whole-brain connectivity patterns with varying degree of sparsity across participants (mean and standard deviation of the proportion of connections present during left-hand movements: 0.32 ± 0.17; and right-hand movements: 0.33 ± 0.17). These sparse connectivity patterns again revealed pronounced functional integration in a widespread network (Fig. 5B). In brief, as expected and consistent with the anatomically constrained analysis, the sparse connectivity patterns revealed pronounced clusters of excitatory connections among regions in the motor (e.g., *A4ul, A6cdl*) and somatosensory cortex (e.g., *A1/2/3ulhf, A2*), occipital lobe (e.g., *mOccG, V5/MT*), as well as parietal cortex (e.g., *A39rd/rv, A40rd/rv, A7m*), and frontal lobe (e.g., *A6vl, A8vl, A44v*). Again, the majority of connections were of positive sign (i.e., excitatory), reflecting the fact that our model describes activity changes relative to rest and that our task induced exclusively positive BOLD activations (i.e., hand movements > rest) but no significant deactivations (i.e., rest > hand movements) when correcting for multiple comparisons. With regard to driving inputs, excitatory effects were observed for regions in the contralateral precentral (*A4ul, A4t, A6cdl*) and postcentral gyrus (*A1/2/3ulhf, A2*). Additionally, we found driving inputs to SMA (*A6m*) and visual regions, including the middle occipital gyrus (*mOccG*) and the motion-sensitive area (*V5/MT*).

As for the tractography-guided application of rDCM, we tested whether the sparse effective connectivity estimates showed asymmetries between afferent and efferent connections. As above, differences in the strength between afferent and efferent connections were comparable in magnitude with the connection strengths themselves (Fig. 5C). This demonstrates that rDCM estimates displayed directedness in the connectivity patterns also when embedded sparsity constraints were used.

For rDCM under sparsity constraints, which in contrast to the anatomically informed analysis does not rely on a symmetric structural connectome, it is instructive to inspect the top 500 connections for both left- and right-hand movements (Fig. 5D-E). This plot illustrates the expected contralateral lateralization of the connectivity pattern – in particular, for connections among pre- and postcentral gyrus, as well as for connections from superior frontal gyrus (e.g., *A6m*) and parietal regions to premotor and motor regions. Finally, for both left- and right-hand movements, one can observe strong interhemispheric connections that were most pronounced among homotopic areas in frontal and parietal cortex.

Similarly, for rDCM with embedded sparsity constraints, one can test the prevalence of bidirectional as compared to unidirectional connections in the inferred functional connectome. We computed the percentage of connections that – if present – also had a reciprocal connection (i.e., not considering cases where both afferent and efferent connections were pruned from the network). Collating over all participants, we found that the majority of connections were reciprocal (left-hand movements: 82%; right-hand movements: 84%). By comparison, estimates for cortical areas in non-human primates that are based on anatomical tract tracing data range between approximately 80–100% (see Fig. 6 in Kötter and Stephan, 2003).

3.3.2. *Mirror symmetry of left- and right-hand movements*

As for the anatomically informed rDCM analysis, we explicitly assessed the effect of hand movement condition (i.e., left vs. right hand). Again, we found the expected mirror-symmetric pattern, with connections in the left hemisphere being increased during right-hand movements and, vice versa, connections in the right hemisphere being increased during left-hand movements (Fig. 6). Significant effects ($p <$ 0.05, FDR-corrected for multiple comparisons across the 43,472 free parameters) were again constrained to connections among sensorimotor regions. We observed an effect of the hand movement condition for the intrahemispheric connections among M1 (*A4ul*), SM1 (*A1/2/3ulhf, A2*), and SMA (*A6m*).

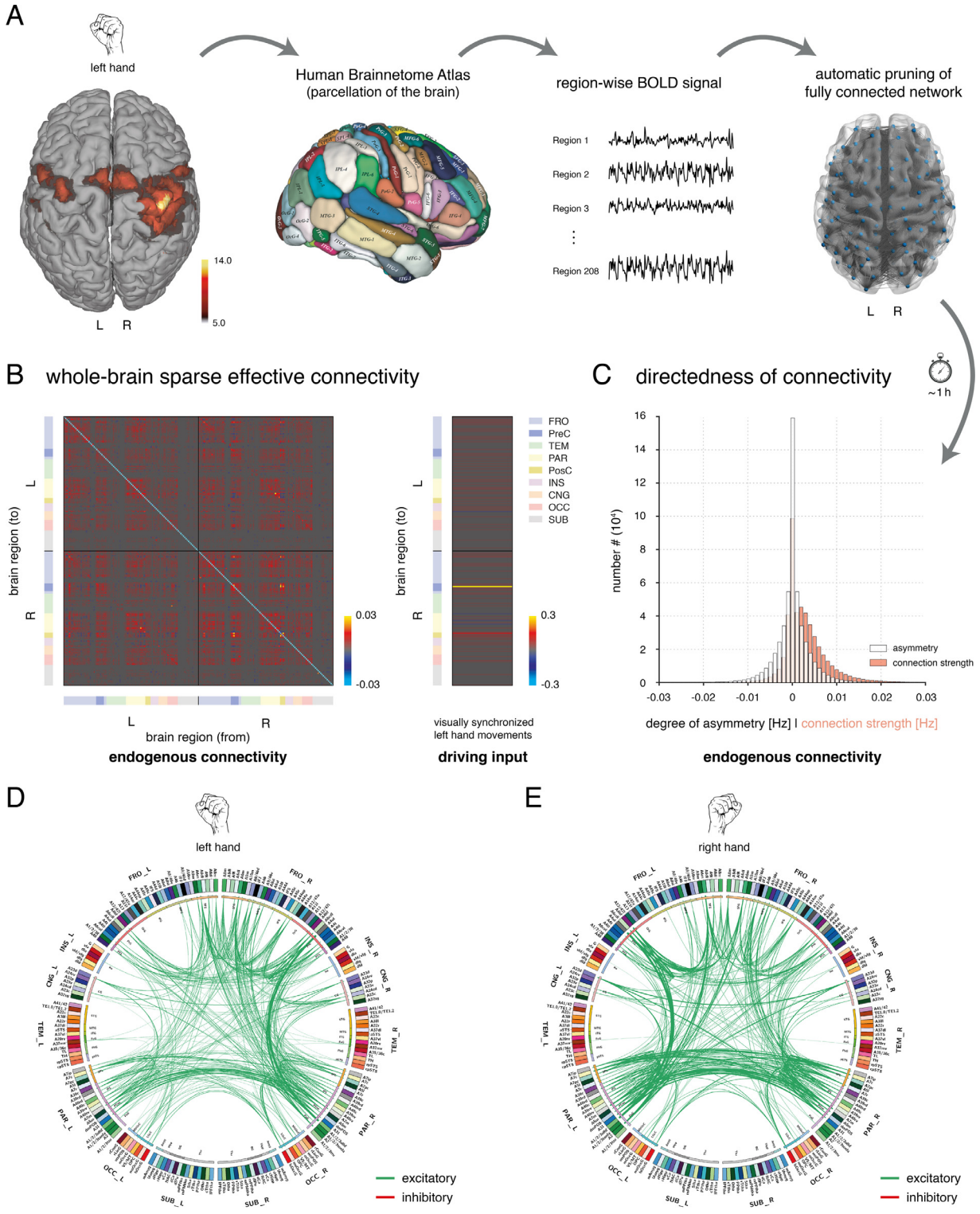

Fig. 5. Sparse whole-brain effective connectivity pattern underlying unilateral hand movements as assessed with rDCM when embedded sparsity constraints were used to prune a fully (all-to-all) connected network. **(A)** For the given BOLD activation pattern during visually synchronized hand movements, the Human Brainnetome atlas (Fan et al., 2016) was used as a whole-brain parcellation scheme. Region-wise BOLD signal time series were extracted for each participant individually as the principal eigenvariate and entered effective connectivity analyses using rDCM. A fully connected network was assumed and then pruned to an optimal (with respect to the negative free energy) degree of sparsity during model inversion. **(B)** Mean posterior parameter estimates for connections (*left*) and driving inputs (*right*) during left-hand movements, averaged across participants. Regions are separated in left hemisphere (L) and right hemisphere (R). For each hemisphere, regions are divided into different sets, including frontal (FRO; *blue*), temporal (TEM; *green*), parietal (PAR; *yellow*), insular (INS; *purple*), cingulate (CNG; *orange*), occipital (OCC; *red*), and subcortical (SUB; *grey*); as specified by the Brainnetome atlas. Additionally, we have explicitly highlighted regions of the precentral gyrus (PreC; *dark blue*) in the frontal lobe, as well as regions of the postcentral gyrus (PosC; *dark yellow*) in the parietal lobe as these are key components of the motor network. The colormap is scaled with respect to the strongest between-region connection. **(C)** Histogram of asymmetry between the afferent (incoming) and efferent (outgoing) part of reciprocal connections (*white*). This suggests that the asymmetry was comparable in magnitude with the connection strengths themselves (*red*). **(D)** Lines represent the 500 connections with the strongest effect for left-hand movements (i.e., highest absolute T value of the two-sided one-sample *t*-test for LH vs. baseline) **(E)** and right-hand movements (i.e., RH vs. baseline). The labels on the outermost ring show the anatomical lobe for each of the nodes: frontal, insula, cingulate, temporal, parietal, occipital, and subcortical. For each brain region defined by the Brainnetome atlas, an abbreviation and color are defined. *L* = left hemisphere; *R* = right hemisphere.

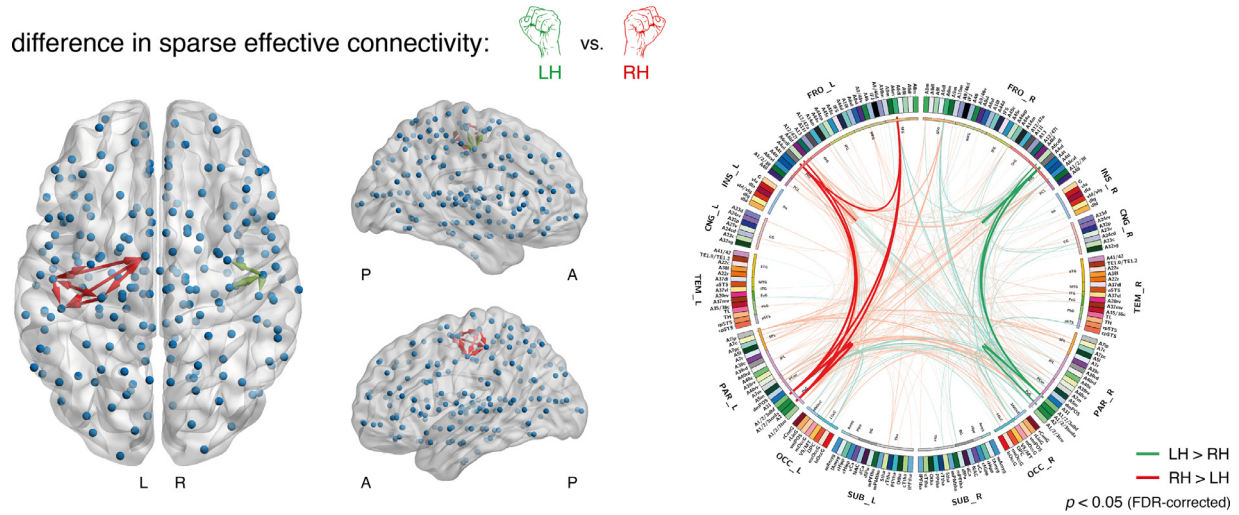

Fig. 6. Mirror symmetry of the effect of hand movement condition (i.e., left vs. right hand) in the motor network as assessed using rDCM with embedded sparsity constraints to prune a fully (all-to-all) connected network. The differential effect of hand movement condition was graphically projected onto a whole-brain volume (*left*). Green arrows indicate connections that were significantly increased during left-hand movements as compared to right-hand movements; red arrows indicate connections that were significantly increased during right-hand movements compared to left-hand movements ($p < 0.05$, FDR-corrected for multiple comparisons). Note that edges in this graphical representation are directed. *L* = left hemisphere; *R* = right hemisphere; *A* = anterior; *P* = posterior. Results can also be inspected when graphically rendered as a connectogram (*right*). Solid lines represent the connections that showed a significant effect of the hand movement condition ($p < 0.05$, FDR-corrected). Lines with faded colors represent the subsequent 500 connections with the strongest differential effect (highest absolute T values of the two-sided paired *t*-test). The labels on the outermost ring show the anatomical lobe for each of the nodes: frontal, insula, cingulate, temporal, parietal, occipital, and subcortical. For each brain region defined by the Brainnetome atlas, an abbreviation and color are defined. Inside the parcellation ring, connections showing a significant effect of the hand movement condition are displayed as edges, with the color code defined as above (i.e., green = LH>RH, red = RH>LH).

3.3.3. Graph-theoretical analyses

In a next step, we applied graph-theoretical measures (Bullmore and Sporns, 2009) to the sparse whole-brain effective connectivity patterns underlying unilateral hand movements. Specifically, using graph theory, we intended to corroborate the pivotal role of motor regions in the pre- and postcentral gyrus during our task, as well as the known hemispheric lateralization of the network. To this end, we chose graph-theoretical measures that capture the importance/relevance of each node and that have frequently been used in the field of connectomics: "betweenness centrality" and "node strength (in & out)". We tested whether graph-theoretical measures would more faithfully reflect known functional properties of the motor system when applied to directed as compared to undirected connectivity measures.

Fig. 7 shows the betweenness centrality for each of the 208 parcels from the Brainnetome atlas (projected onto a whole-brain volume) for left- and right-hand movements. The expected contralateral dominance of the motor regions is clearly visible: For left-hand movements, the node with the highest betweenness centrality was right M1; whereas, for right-hand movements, left M1 showed one of the highest betweenness centrality scores (Fig. 7A-B). We also found high betweenness centrality scores during unilateral hand movements in regions located in the contralateral somatosensory cortex (*A1/2/3ulhf, A2*). Furthermore, high betweenness centrality in both left and right hemisphere, regardless of the hand movement condition, was observed in the medial area 7 (*A7m*), which represents the visuospatial/-motor part of the precuneus.

Hemispheric differences in betweenness centrality revealed the expected mirror-symmetric pattern within motor-related regions in the precentral (*A4ul*) and postcentral gyrus (*A1/2/3ulhf, A2*). Specifically, hemispheric asymmetry in these regions depended strongly on the hand movement condition (Fig. 7C-D): betweenness centrality was higher in the right hemisphere during left-hand movements, and higher in the left hemisphere during right-hand movements.

Notably, the mirror symmetry of functional integration during left- and right-hand movements was not a global finding, but was specific to the motor network. In contrast, regions in the frontal (e.g., *A6dl, A46, A8vl, A44d*) and parietal lobe (e.g., *A7r*) showed higher betweenness centrality in the right hemisphere, regardless of the hand movement condition. Furthermore, regions in the occipital lobe, such as the primary visual cortex in the occipital polar cortex (*OPC*) and the motion sensitive area *V5/MT*, did not show marked hemispheric asymmetries, consistent with the central visual stimulation during both hand movement conditions.

For node strength, results were highly consistent with the pattern observed for betweenness centrality, again highlighting the contralateral dominance of motor regions and the expected mirror symmetry of the network for left- and right-hand movements (Supplementary Figure S2).

3.3.4. Sparsity constraints vs anatomical constraints

In a final step, we compared the two general modes of operation for rDCM: fixed network architecture informed by a structural connectome (anatomical constraints) versus pruning a fully connected whole-brain model (sparsity constraints). First, one can observe that the effective connectivity pattern under anatomical constraints (Fig. 3B) is not dissimilar to the product of the fixed Brainnetome structural connectome serving as prior (Fig. 1A) and the inferred pattern under sparsity constraints (Fig. 5B), which intuitively is plausible. Second, since rDCM provides a principled measure of model goodness, the log model evidence, one can use BMS to ask which mode provided a better explanation of the data. Random effects BMS indicated that the model with anatomically informed (fixed) network architecture was superior with a protected exceedance probability of 1. This suggests that – in this case – exploiting available anatomical information to inform the architecture of the model was clearly beneficial.

3.4. Computational burden

Concerning computational efficiency, running model inversion on a single processor core (without parallelization) on the Euler cluster at ETH Zurich (https://scicomp.ethz.ch/wiki/Euler), rDCM took on the order of a minute or less when assuming structurally fixed connectivity and input structure. More specifically: for models 1 and 2 (16,868 free

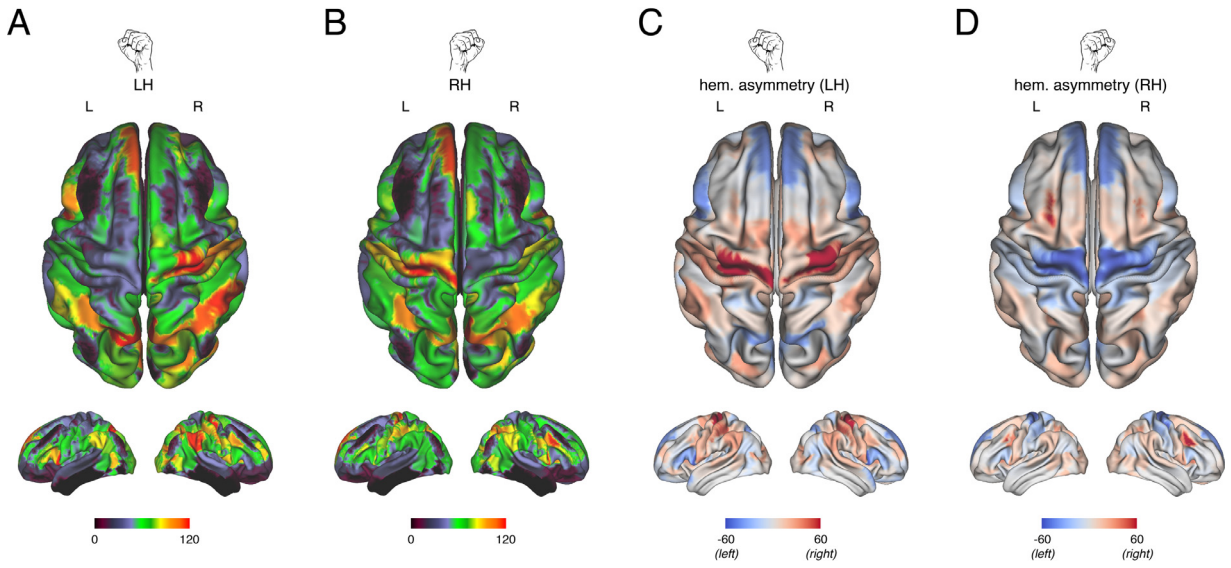

Fig. 7. Graph-theoretical analysis of the whole-brain effective connectivity patterns underlying unilateral hand movements as inferred using rDCM when embedded sparsity constraints were used to prune a fully (all-to-all) connected network. Betweenness centrality was evaluated for each parcel of the Human Brainnetome atlas for **(A)** left-hand and **(B)** right-hand fist closings and then graphically projected onto a whole-brain volume. **(C)** Hemispheric asymmetries in betweenness centrality for left-hand fist closings. Hemispheric asymmetries were assessed by evaluating the difference in betweenness centrality for homotopic parcels in the left and right hemisphere. Positive values (*red*) indicated right-hemispheric dominance in betweenness centrality for a set of homotopic parcels, whereas negative values (*blue*) indicated left-hemispheric dominance in betweenness centrality for a set of homotopic parcels. **(D)** Hemispheric asymmetries in betweenness centrality for right-hand fist closings. Again, this clearly illustrates the mirror symmetry of the motor network in the pre- and postcentral gyrus. Betweenness centrality for directed and weighted adjacency matrices was computed using the Brain Connectivity toolbox (Rubinov and Sporns, 2010), which is freely available (https://sites.google.com/site/bctnet/). Betweenness centrality values for each parcel were visualized using the Human Connectome Workbench, also publicly available (https://www.humanconnectome.org/software/connectome-workbench). *L* = left hemisphere; *R* = right hemisphere; LH = left hand; RH = right hand.

parameters), model inversion took around 20 s, whereas for model 3 (43,472 free parameters), model inversion took roughly 100 s.

Using sparsity constraints to prune fully connected networks is computationally more demanding: on average (across participants), rDCM took roughly 4 h on a single processor core to infer sparse connectivity patterns under a given p_0^i value. This compares favorably to other methods of large-scale effective connectivity, like cross-spectral DCM, for which 21–42 h of run-time on a high-performance computing cluster for a network with 36 regions and 1260 connections has been reported (Razi et al., 2017).

Notably, these run-times were obtained using a language not optimized for speed (Matlab) nor without any effort to speed the code up by parallelization. The latter is a straightforward and powerful option to further enhance the efficiency of rDCM (Frässle et al., 2018a). This is due to the mean field approximation in rDCM which allows applying the VB update equations to each region independently. Specifically, when using 16 processor cores in parallel, the above run-time for inferring sparse effective connectivity patterns could be reduced to around 40 min on average. The values reported here should only be treated as a rough indication, as run-times will depend on the specific hardware used.

3.5. Comparison to undirected measures of brain connectivity

In a final step, we compared the whole-brain effective connectivity estimates with measures of functional connectivity, which represent the current standard in human connectomics. For this, we computed for each participant Pearson correlation coefficients between exactly the same 208 BOLD signal time series as used in the rDCM analysis. Pearson correlations arguably represent the simplest and most widely used measures of functional connectivity. In contrast to the Bayesian framework of rDCM, Pearson correlations are not subject to any regularization, which has advantages and disadvantages: they might be more sensitive for detecting functional coupling, but are also very sensitive to measurement noise (Friston, 2011).

Functional connectivity patterns for the unilateral hand movements were qualitatively similar to the effective connectivity patterns obtained using rDCM: we observed coupling among motor (i.e., precentral, SMA), visual (occipital), somatosensory/proprioceptive (postcentral, parietal) and frontal regions (Fig. 8A). However, in contrast to effective connectivity (cf. Fig. 3C and 5B), functional connectivity does not afford any information on the directionality of influences, leading to symmetric connectivity matrices.

We then tested for the differential effect of the hand movement condition (i.e., left vs. right hand) using two-sided paired *t*-tests ($p < 0.05$, FDR-corrected) after Fisher r-to-z transformation of the correlation coefficients. Consistent with rDCM, intrahemispheric functional connectivity among M1 (*A4ul*) and SM1 (*A1/2/3ulhf, A2*) of the contralateral hemisphere was increased (Fig. 8B). However, functional connectivity did not show the expected mirror-symmetric pattern within the motor network as clearly as in the case of rDCM: Various connections within the motor network (and beyond) showed the opposite effect, resulting in a more ambiguous pattern. Furthermore, no significant effect could be observed for connections between SMA (*A6m*) and regions in the pre- and postcentral gyrus when correcting for multiple comparisons. This was slightly unexpected given the prominent role of the SMA in the initiation of voluntary hand movements (Grefkes et al., 2008; Rao et al., 1993).

To compare functional and effective connectivity estimates more directly, we computed a congruence map between functional connectivity and rDCM, covering the 500 connections with the strongest effect of the hand movement condition (for details, see legend to Fig. 8C). While the majority of connections did not overlap between the two methods, those connections that showed strong differences between hand conditions (mainly connections among motor-related regions) displayed the same sign for functional connectivity and rDCM estimates (Fig. 8C). This indicates that, at the level of undirected connections, functional and

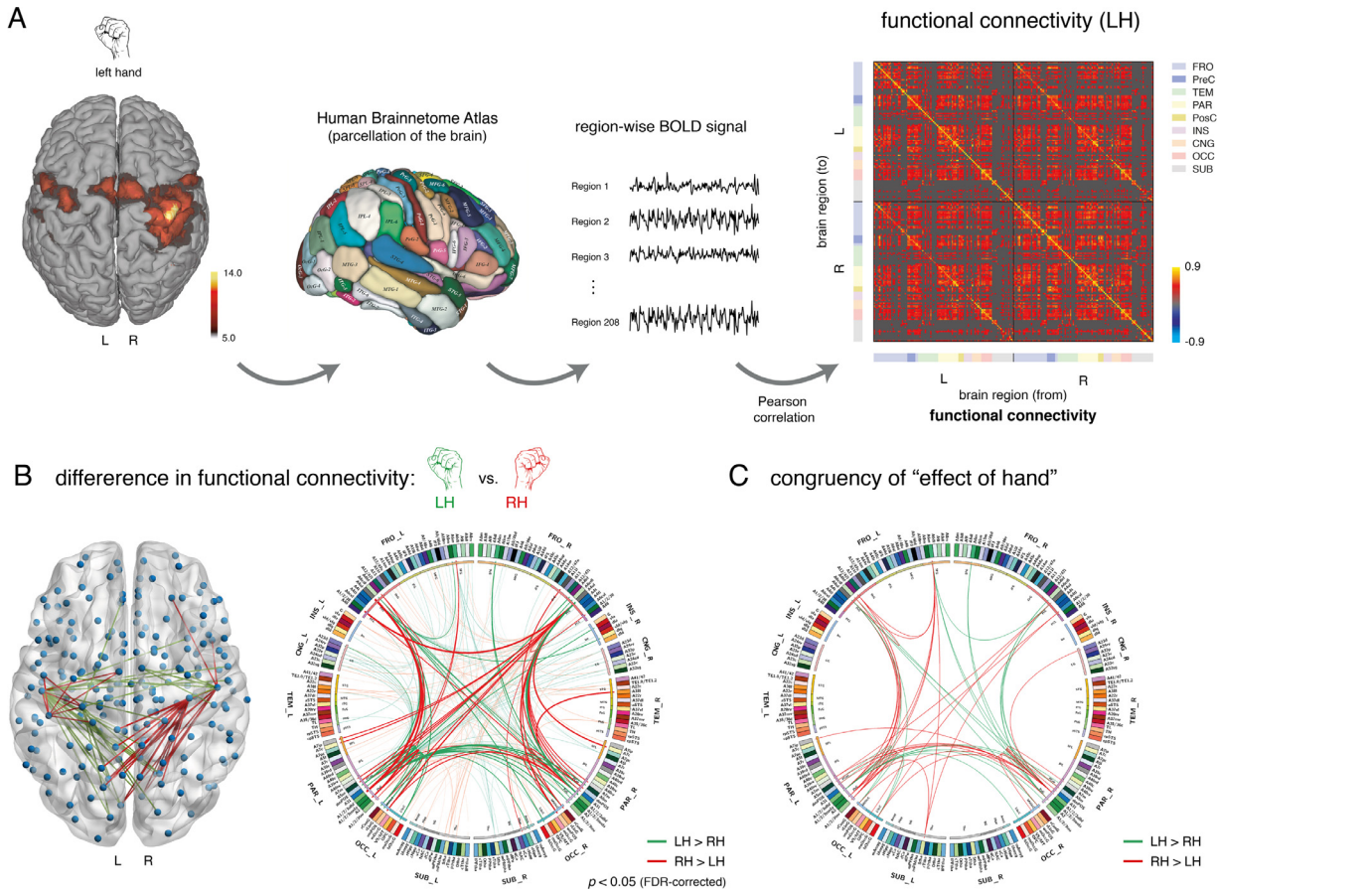

Fig. 8. Functional connectivity pattern underlying unilateral hand movements as assessed using the Pearson correlation coefficient among the same BOLD signal time series as utilized for the rDCM analysis. **(A)** For the given BOLD activation pattern during visually synchronized hand movements, the Human Brainnetome atlas (Fan et al., 2016) was used as a whole-brain parcellation scheme. Region-wise BOLD signal time series were extracted for each participant individually as the principal eigenvariate and entered functional connectivity analyses using the Pearson correlation coefficients. To allow for comparability with rDCM results, the functional connectivity matrix is thresholded such that the sparsity of the matrix resembles the sparsity of the structural connectome from the Brainnetome atlas. Here shown is the mean functional connectivity matrix, averaged across participants. Regions are separated in left hemisphere (L) and right hemisphere (R). For each hemisphere, regions are divided into different sets, including frontal (FRO; *blue*), temporal (TEM; *green*), parietal (PAR; *yellow*), insular (INS; *purple*), cingulate (CNG; *orange*), occipital (OCC; *red*), and subcortical (SUB; *grey*); as specified by the Brainnetome atlas. Additionally, we have explicitly highlighted regions of the precentral gyrus (PreC; *dark blue*) in the frontal lobe, as well as regions of the postcentral gyrus (PosC; *dark yellow*) in the parietal lobe as these are key components of the motor network. The colormap is scaled with respect to the strongest between-region connection. **(B)** Differential effect of hand movement condition on functional connectivity, projected onto a whole-brain volume (*left*). Green lines indicate connections that were significantly increased during left-hand movements as compared to right-hand movements; red lines indicate connections that were significantly increased during right-hand movements compared to left-hand movements ($p < 0.05$, FDR-corrected). *L* = left hemisphere; *R* = right hemisphere; LH = left hand; RH = right hand. Results can also be rendered as a connectogram (*right*). Solid lines represent significant differential effects ($p < 0.05$, FDR-corrected), faded colors represent the 500 connections with the next highest absolute T values of the two-sided paired *t*-test. The labels on the outermost ring show the anatomical lobe for each of node: frontal, insula, cingulate, temporal, parietal, occipital, and subcortical. Next, abbreviation and color for each region are shown. **(C)** Connections showing a congruent effect of hand movement condition on the functional and effective connectivity estimates. Congruency was established by logical AND of the connectomes in Figs. 4 and 8B, where rDCM estimates were first converted into undirected connections before binarizing all connections as having positive and negative strengths. Lines indicate those of the top 500 connections of the functional and effective connectivity patterns that showed the same differential hand movement effect (i.e., LH>RH or RH>LH).

effective connectivity estimates are qualitatively compatible for those connections that are expected to be most relevant for the task.

We repeated the graph-theoretical analyses by evaluating betweenness centrality and node strength for the undirected functional connectivity patterns. In contrast to effective connectivity, functional connectivity did not show the expected pattern of betweenness centrality. Specifically, motor-related regions in the contralateral precentral (*A4ul*) and postcentral gyrus (*A1/2/3ulhf, A2*) did not yield high betweenness centrality scores (Fig. 9A-B), in contradiction to their established role during unilateral hand movements. Furthermore, when testing for hemispheric differences in betweenness centrality, we did not observe the expected mirror symmetry in the motor network (Fig. 9C-D). Similarly, node strength did not capture the importance of motor-related regions and yielded counterintuitive hemispheric asymmetries (Supplementary Figure S3), with a node strength pattern of motor-related regions opposite to what one would expect. This result may have been driven by connections between motor and more occipital regions that showed unexpected effects of hand in the functional connectivity analyses (Fig. 8B). These unexpected findings may reflect the known sensitivity of correlation-based functional connectivity estimates to measurement noise (Friston, 2011).

Finally, at the request of a reviewer, we have repeated all functional connectivity analyses using regularized partial correlations (instead of Pearson's correlations). To this end, we computed for each participant partial correlations between the same 208 BOLD signal time series as used in the previous analyses. Consistent with the approach reported in Smith et al. (2011), we here used an open-source MATLAB implementation referred to as "L1precision"

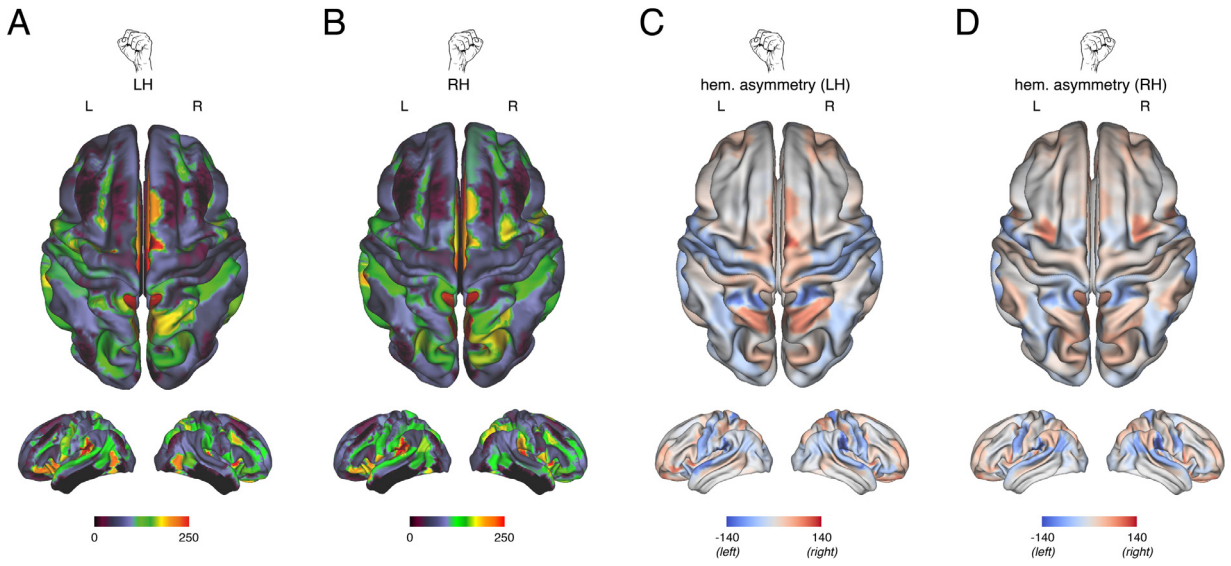

Fig. 9. Graph-theoretical analysis of the whole-brain functional connectivity patterns during unilateral hand movements as assessed using the Pearson correlation coefficient. Betweenness centrality was evaluated for each parcel of the Human Brainnetome atlas for **(A)** left-hand and **(B)** right-hand fist closings and then graphically projected onto a whole-brain volume. **(C)** Hemispheric asymmetries in betweenness centrality for left-hand fist closings. Hemispheric asymmetries were assessed by evaluating the difference in betweenness centrality for homotopic parcels in the left and right hemisphere. Positive values (*red*) indicated right-hemispheric dominance in betweenness centrality for a set of homotopic parcels, whereas negative values (*blue*) indicated left-hemispheric dominance in betweenness centrality for a set of homotopic parcels. **(D)** Hemispheric asymmetries in betweenness centrality for right-hand fist closings.

(https://www.cs.ubc.ca/~schmidtm/Software/L1precision.html) to compute the regularized inverse covariance matrix, from which the regularized partial correlation matrix can be computed (Whittaker, 1990). In this implementation, regularization is achieved by placing a Laplace prior (i.e., L1-regularizer of the negative log-likelihood) on the values of the inverse covariance matrix (or precision matrix), following the procedure described by Friedman et al. (2008) as the Graphical Lasso or GLasso.

In summary, regularized partial correlation patterns for the unilateral hand movements were qualitatively similar to the patterns obtained with rDCM and Pearson's correlations. Specifically, partial correlations showed coupling among the aforementioned motor-related regions (Supplementary Figure S4A). Interestingly, by far the strongest partial correlations were observed amongst BOLD signal time series from homotopic brain regions in both hemispheres. Having said this, overall, associations were much weaker as compared to Pearson's correlations. As for the previous functional connectivity analysis, partial correlations do not afford information on the directionality of influences, leading to symmetric connectivity matrices. The differential effect of the hand movement condition (i.e., left vs. right hand) showed the expected effect on intrahemispheric functional connections among M1 (*A4ul*) and SM1 (*A1/2/3ulhf*), consistent with rDCM and Pearson's correlations (Supplementary Figure S4B). However, partial correlations were less sensitive in delineating the effect of the hand movement condition and, similar to Pearson's correlations, did not show the expected mirror-symmetric pattern within the motor network as clearly as in the case of rDCM. Finally, the graph-theoretical analyses (i.e., betweenness centrality and node strength) were somewhat more similar to the results obtained from effective connectivity analyses as compared to Pearson's correlations. Specifically, regularized partial correlations did reveal the expected mirror symmetry in the motor network for betweenness centrality (Supplementary Figure S5); yet, this was less clear for node strength (Supplementary Figure S6). Furthermore, neither of the two graph-theoretical measures revealed high scores for motor-related regions in the contralateral precentral (*A4ul*) and postcentral gyrus (*A1/2/3ulhf, A2*), which is in contradiction to their established role during unilateral hand movements.

4. Discussion

In this paper, we assessed the construct validity of regression DCM (rDCM) for inferring whole-brain effective connectivity patterns from fMRI data. Using a hand movement dataset, we demonstrated that rDCM can infer plausible effective connectivity patterns in a network comprising over 200 regions and 40,000 free parameters. Furthermore, we applied graph-theoretical measures to the whole-brain effective connectivity patterns and demonstrate that they capture the expected pivotal role of motor-related regions, as well as the hemispheric asymmetries of the network.

In brief, rDCM identified pronounced functional integration among key components of the motor network – e.g., M1, SM1, and SMA. Furthermore, when testing for effects of the hand movement condition (i.e., left vs. right hand), we found the expected mirror-symmetric pattern: connections among key motor regions in the left hemisphere were stronger during right-hand movements and, vice versa, connections in the right hemisphere were stronger during left-hand movements. This pattern could not only be obtained when structural connectivity data were used to inform the network architecture of the whole-brain DCMs, but even in the case of complete absence of *a priori* assumptions about the network's architecture by automatically pruning fully connected graphs to an optimal degree of sparsity.

However, our method also failed to detect a characteristic of the motor system that has been reported previously: interhemispheric inhibition of the ipsilateral M1 by the contralateral M1 during unilateral hand movements (Ferbert et al., 1992). This may be due to the fact that hand movements of different conditions were separated into two scanning sessions, potentially rendering interhemispheric inhibition less critical as in paradigms that alternate between the two conditions (Grefkes et al., 2008).

We further demonstrated the application of graph-theoretical measures to the inferred whole-brain effective connectivity patterns. Specifically, we show that measures that capture the relevance of a network node, i.e., betweenness centrality and node strength, correctly identify motor-related regions in the pre- and postcentral gyrus as key components of the network and show the expected hemispheric asymme-

try (Levy, 1969; Roland and Zilles, 1996). Furthermore, our graph-theoretical analyses are consistent with known functional characteristics of the human brain, including the relevance of precuneus in directing spatial attention during preparation and execution of motor actions (Cavanna and Trimble, 2006; Kawashima et al., 1995; Wenderoth et al., 2005) and its role as a central "small-world network" hub (Bullmore and Sporns, 2009). Similarly, our analyses revealed the expected right-hemispheric lateralization of the fronto-parietal network underlying visuospatial attention (Fink et al., 2000; Mesulam, 1981).

Recently, graph theory has found widespread application in neuroscience and has provided valuable insights into the organization of the brain (Bullmore and Sporns, 2009; Fornito et al., 2013; Rubinov and Sporns, 2010). However, to render graph-theoretical approaches, and connectomics in general, meaningful for understanding organizational principles in large-scale networks, individual connection estimates need to be neurobiologically interpretable. For instance, estimates need to capture functional asymmetries of reciprocal connections – e.g., differences between ascending and descending connections in cortical hierarchies (Felleman and Van Essen, 1991; Zeki and Shipp, 1988) or asymmetries in interhemispheric interactions (Frässle et al., 2016; Gazzaniga, 2000; Stephan et al., 2007). This is not the case for currently used standard measures of connectivity in humans, such as DWI-derived structural connectivity and fMRI-based functional connectivity. These measures are undirected and thus do not capture functional asymmetries of reciprocal connections. Extending graph-theoretical approaches to effective (directed) connectivity may therefore be critical for exploiting the information provided by graph-theoretical indices and for providing a more faithful assessment of the network topology underlying brain dynamics. Indeed, our findings suggest that directed estimates of connectivity boost the explanatory power of network analyses: graph theory applied to rDCM estimates better match known functional roles of key motor regions than when undirected functional connectivity estimates are used.

We would have liked to report a comparison between rDCM and measures of directed functional connectivity, like multivariate Granger causality (GC; Roebroeck et al., 2005). However, for the data used here, conditional GC estimates obtained using the "Causal Connectivity Analysis" toolbox (Seth, 2010) did not show convergence, possibly due to issues like TR and the relatively short scanning time (i.e., low number of data points per region) (Roebroeck et al., 2005; Seth et al., 2013). By contrast, the feasibility of obtaining meaningful estimates by rDCM underscores its potential suitability for clinical applications, where long scanning sessions are usually not possible.

Our results suggest that rDCM confers important practical advantages for human connectomics and network neuroscience. Several strengths and innovations are worth highlighting. First, rDCM provides different modes of operation for deriving directed connectivity fingerprints: it can exploit subject-specific anatomical connectivity information for constraining inference; alternatively, when no such information is available, rDCM can infer optimally sparse representations of whole-brain networks. Second, by introducing sparsity constraints, rDCM circumvents the need for arbitrary thresholding of connectivity matrices. Instead, rDCM yields an optimal degree of sparsity by maximizing the model evidence. Finally, rDCM is computationally highly efficient with run-times on the order of minutes for a fixed network architecture and few hours when using sparsity constraints per subject. This efficiency renders rDCM a promising tool for clinical applications but also for time-consuming analyses of large-scale datasets like the Human Connectome Project (Van Essen et al., 2013). These developments provide exciting new opportunities for moving human connectomics and network neuroscience towards directed measures of functional integration. Furthermore, rDCM may find useful application in the emerging fields of Computational Psychiatry and Computational Neurology where computational readouts of directed connectivity in whole-brain networks are of major relevance. For instance, in schizophrenia, the "dysconnection hypothesis" postulates that impairments in neuromodulatory regulation of NMDA receptor dependent synaptic plasticity lead to dysconnectivity, particularly in circuits for perception and learning (Friston et al., 2016; Friston, 1998; Stephan et al., 2006, 2009a). Similarly, for other psychiatric disorders like depression or autism, global dysconnectivity has been suggested as a hallmark of the disease, which points to the clinical utility of whole-brain models of directed connectivity (Deco and Kringelbach, 2014; Frässle et al., 2018b; Menon, 2011; Stephan et al., 2015).

Despite these strengths, our study is also subject to limitations. First, the Brainnetome atlas does not cover the cerebellum (Fan et al., 2016), which plays an important role in preparation and execution of motor actions (Witt et al., 2008). This is similar to most other state-of-the-art whole-brain parcellation schemes, like the Human Connectome Project parcellation (HCP MMP 1.0; Glasser et al., 2016), which are equally restricted to cortical regions (although recent work has extended the Glasser atlas to subcortical structures as well; see Ji et al., 2019). Other parcellation schemes, such as the Automated Anatomical Labeling (AAL) atlas, do include the cerebellum but have other shortcomings. For example, purely anatomically defined parcellations like the AAL atlas delineate areas based on macroscopic landmarks only (Tzourio-Mazoyer et al., 2002). Similarly, atlases that derive from tractography or cytoarchitecture provide more fine-grained parcellations, while still neglecting functional information. For the present analysis, we deliberately focused on the cortex and chose the Brainnetome atlas for three reasons: (i) the atlas is sufficiently fine-grained to allow for meaningful large-scale effective connectivity analyses among cortical regions, (ii) has been demonstrated to provide robust parcels across the population as assessed using cross-validation, and (iii) provides not only a parcellation of the brain but also tractography-based information on how these parcels are anatomically connected (which informed the network architecture in our initial rDCM analysis).

Second, rDCM is still in an early development stage and the current implementation is subject to methodological limitations (Frässle et al., 2018a, 2017). In particular, the biophysically plausible hemodynamic model in classical DCM was replaced with a fixed HRF. Consequently, rDCM presently does not capture variability in the BOLD signal across regions and individuals. In this work, we accounted for variability in latency and duration of the hemodynamic responses by including temporal and dispersion derivatives of the canonical HRF as confound regressors in the GLM (Friston et al., 1998). Nevertheless, replacing the fixed HRF with a flexible hemodynamic model represents a major future development of rDCM.

It is worth highlighting that rDCM is not the only approach that aims to infer effective connectivity in large-scale networks. Alternative approaches include BNMs (Deco et al., 2013) and cross-spectral DCMs (Razi et al., 2017). BNMs combine biophysical mean-field models of the local neuronal dynamics with long-range connections informed by structural connectivity estimates. However, the complexity of these models renders parameter estimation computationally extremely challenging, restricting applications to relatively few free parameters (Deco et al., 2014a, 2014b; Demirtas et al., 2019); but see Wang et al. (2019) for notable progress in this area. A platform for constructing and applying BNMs to a variety of neuroimaging modalities is the Virtual Brain (Jirsa et al., 2010).

Recently, a large-scale network model has been introduced that also enables inference on individual connectivity parameters (Gilson et al., 2017). Here, local dynamics of brain regions are described by an Ornstein-Uhlenbeck process. This model further differs from rDCM in that effective connectivity is not estimated within a Bayesian framework but by maximum likelihood, which does not enable automatic pruning of fully connected networks. For "resting-state" data, a variant of cross-spectral DCM has been proposed, where the effective number of free parameters is reduced by constraining the prior covariance matrix (Razi et al., 2017). In contrast to rDCM, cross-spectral DCM explicitly captures regional variability in hemodynamic responses (Friston et al., 2000). However, this increase in physiological realisms comes at the ex-

pense of non-optimal computational efficiency – resulting in run-times between 21 and 42 h for a single DCM with 36 regions (Razi et al., 2017). Hence, in its current implementation, cross-spectral DCM is unlikely to scale to whole-brain networks with hundreds of regions. In addition to cross-spectral DCM, alternative variants of large-scale connectivity analyses for "resting-state" fMRI data have recently been proposed that are inspired by rDCM and pursue a sparsity-inducing approach (Prando et al., 2019).

Besides DCM and BNM, other approaches that infer directed interactions in large-scale networks include MVGC (Goebel et al., 2003; Roebroeck et al., 2005; Seth, 2010), MINDy (Singh et al., 2020), correlation generalizations (Xu et al., 2017), GIMME (Gates et al., 2014), Bayes nets (Mumford and Ramsey, 2014; Ramsey et al., 2017; Sanchez-Romero et al., 2019), and non-Gaussian models (Sanchez-Romero et al., 2018). A direct comparison of rDCM with a subset of these approaches was recently presented by Frässle et al. (2018a) for synthetic data where the ground truth (i.e., the data-generating model parameters and network architecture) was known. In these simulations, rDCM outperformed, in most cases, other directed connectivity methods, including (i) MVGC (Seth, 2010), (ii) the Fast Adjacency Skewness (FASK; Sanchez-Romero et al., 2018) algorithm as a variant of non-Gaussian methods, and (iii) the Fast Greedy Equivalence Search (FGES; Chickering, 2003; Ramsey et al., 2017, 2010) algorithm as a case of Bayes nets. Having said this, more validation work can still be done. In future work, we would therefore like to compare rDCM to other emerging approaches of whole-brain effective connectivity in application to empirical datasets.

In summary, in comparison to other methods for inferring effective connectivity in large-scale networks, rDCM provides estimates of the full posterior distributions of individual connection strengths in networks with hundreds of nodes, with run-times on the order of minutes for a fixed network architecture and a few hours when using sparsity constraints on standard hardware. It allows for parallelization and scales gracefully (polynomially, as opposed to exponentially) with the number of regions, an important property as methodological advances allow for increasingly fine-grained parcellations of human cortex (Eickhoff et al., 2018). Furthermore, its Bayesian formulation allows for a natural connection to subject-specific anatomical connectivity data (e.g., tractography). Finally, its speed and ability to prune whole-brain networks in the absence of anatomical connectivity information are important assets for clinical applications, potentially supporting time-sensitive clinical assessments with interpretable sparse whole-brain connectograms solely based on fMRI data.

Code and data availability

A Matlab implementation of the regression dynamic causal modeling (rDCM) approach is available as open source code in the **T**ranslational **A**lgorithms for **P**sychiatry-**A**dvancing **S**cience (TAPAS) Toolbox (www.translationalneuromodeling.org/software). Furthermore, following acceptance of this paper, we will publish the code for the analysis as well as the data used in this paper online as part of an online repository that conforms to the FAIR (Findable, Accessible, Interoperable, and *Re*-usable) data principles.

Author contributions

ZMM, KPP and KES conceptualized and designed the study, ZMM and LK performed the experiment, SF co-developed the modeling approach utilized in this study, SF and CTD preprocessed the data, SF analyzed the data, CTD performed a code review of the analysis pipeline, SF and KES discussed and interpreted the results, SF and KES wrote the manuscript, ZMM, CTD, LK, and KPP edited and approved the manuscript.

Declaration of Competing Interest

We confirm that there are no conflicts of interest associated with this publication and that there has been no financial support for this work that could have influenced its outcome.

Further, we confirm that the manuscript has been read and approved by all authors and that there are no other persons who satisfied the criteria for authorship but are not listed. We confirm that the order of authors listed in the manuscript has been approved by all of us.

We confirm that we have given due consideration to the protection of intellectual property associated with this work and that there are no impediments to publication, including the timing of publication, with respect to intellectual property. In so doing we confirm that we have followed the regulations of our institutions concerning intellectual property.

We further confirm that any aspect of the work covered in this manuscript that has involved human subjects has been conducted with the ethical approval of all relevant bodies.

We understand that the Corresponding Author is the sole contact for the Editorial process (including Editorial Manager and direct communications with the office). He is responsible for communicating with the other authors about progress, submission of revisions and final approval of proofs. We confirm that we have provided a current, correct email address which is accessible by the Corresponding Author.

Acknowledgments

This work was supported by the UZH Forschungskredit Postdoc (SF), the ETH Zurich Postdoctoral Fellowship Program and the Marie Curie Actions for People COFUND Program (SF), the René and Susanne Braginsky Foundation (KES), the Swiss National Science Foundation 320030_179377 (KES), and the University of Zurich (KES).

Supplementary materials

Supplementary material associated with this article can be found, in the online version, at doi:10.1016/j.neuroimage.2020.117491.

References

Baker, J.T., Dillon, D.G., Patrick, L.M., Roffman, J.L., Brady Jr., R.O., Pizzagalli, D.A., Ongur, D., Holmes, A.J., 2019. Functional connectomics of affective and psychotic pathology. Proc. Natl. Acad. Sci. U. S. A. 116, 9050–9059.

Balchandani, P., Naidich, T.P., 2015. Ultra-high-field MR neuroimaging. AJNR Am. J. Neuroradiol. 36, 1204–1215.

Bassett, D.S., Sporns, O., 2017. Network neuroscience. Nat. Neurosci. 20, 353–364.

Bielczyk, N.Z., Uithol, S., van Mourik, T., Anderson, P., Glennon, J.C., Buitelaar, J.K., 2019. Disentangling causal webs in the brain using functional magnetic resonance imaging: a review of current approaches. Netw. Neurosci. 3, 237–273.

Bishop, C.M., 2006. Pattern recognition and machine learning. Springer, New York. 12, 13, 47, 105.

Brandes, U., 2001. A faster algorithm for betweenness centrality. J. Math. Sociol. 25, 163–177.

Buckholtz, J.W., Meyer-Lindenberg, A., 2012. Psychopathology and the human connectome: toward a transdiagnostic model of risk for mental illness. Neuron 74, 990–1004.

Bullmore, E., Sporns, O., 2009. Complex brain networks: graph theoretical analysis of structural and functional systems. Nat. Rev. Neurosci. 10, 186–198.

Cavanna, A.E., Trimble, M.R., 2006. The precuneus: a review of its functional anatomy and behavioural correlates. Brain 129, 564–583.

Chickering, D., 2003. Optimal structure identification with greedy search. J. Mach. Learn. Res. 3, 507–554.

Craddock, R.C., Jbabdi, S., Yan, C.G., Vogelstein, J.T., Castellanos, F.X., Di Martino, A., Kelly, C., Heberlein, K., Colcombe, S., Milham, M.P., 2013. Imaging human connectomes at the macroscale. Nat. Methods 10, 524–539.

Deco, G., Jirsa, V.K., McIntosh, A.R., 2013. Resting brains never rest: computational insights into potential cognitive architectures. Trends Neurosci. 36, 268–274.

Deco, G., Kringelbach, M.L., 2014. Great expectations: using whole-brain computational connectomics for understanding neuropsychiatric disorders. Neuron 84, 892–905.

Deco, G., McIntosh, A.R., Shen, K., Hutchison, R.M., Menon, R.S., Everling, S., Hagmann, P., Jirsa, V.K., 2014a. Identification of optimal structural connectivity using functional connectivity and neural modeling. J. Neurosci. 34, 7910–7916.

Deco, G., Ponce-Alvarez, A., Hagmann, P., Romani, G.L., Mantini, D., Corbetta, M., 2014b. How local excitation-inhibition ratio impacts the whole brain dynamics. J. Neurosci. 34, 7886–7898.

Demirtas, M., Burt, J.B., Helmer, M., Ji, J.L., Adkinson, B.D., Glasser, M.F., Van Essen, D.C., Sotiropoulos, S.N., Anticevic, A., Murray, J.D., 2019. Hierarchical heterogeneity across human cortex shapes large-scale neural dynamics. Neuron 101, 1181–1194 e1113.

Edelstein, W.A., Glover, G.H., Hardy, C.J., Redington, R.W., 1986. The intrinsic signal–to-noise ratio in NMR imaging. Magn. Reson. Med. 3, 604–618.

Eickhoff, S.B., Yeo, B.T.T., Genon, S., 2018. Imaging-based parcellations of the human brain. Nat. Rev. Neurosci. 19, 672–686.

Evarts, E.V., 1981. Role of motor cortex in voluntary movements in primates. In: Handbook of Neurophysiology. American Physiological Society, Bethesda, MD, pp. 1083–1120.

Fan, L., Li, H., Zhuo, J., Zhang, Y., Wang, J., Chen, L., Yang, Z., Chu, C., Xie, S., Laird, A.R., Fox, P.T., Eickhoff, S.B., Yu, C., Jiang, T., 2016. The human brainnetome atlas: a new brain atlas based on connectional architecture. Cereb. Cortex 26, 3508–3526.

Feinberg, D.A., Setsompop, K., 2013. Ultra-fast MRI of the human brain with simultaneous multi-slice imaging. J. Magn. Reson. 229, 90–100.

Felleman, D.J., Van Essen, D.C., 1991. Distributed hierarchical processing in the primate cerebral cortex. Cereb. Cortex 1, 1–47.

Ferbert, A., Priori, A., Rothwell, J.C., Day, B.L., Colebatch, J.G., Marsden, C.D., 1992. Interhemispheric inhibition of the human motor cortex. J. Physiol. 453, 525–546.

Fink, G.R., Marshall, J.C., Shah, N.J., Weiss, P.H., Halligan, P.W., Grosse-Ruyken, M., Ziemons, K., Zilles, K., Freund, H.J., 2000. Line bisection judgments implicate right parietal cortex and cerebellum as assessed by fMRI. Neurology 54, 1324–1331.

Fornito, A., Zalesky, A., Breakspear, M., 2013. Graph analysis of the human connectome: promise, progress, and pitfalls. Neuroimage 80, 426–444.

Fornito, A., Zalesky, A., Breakspear, M., 2015. The connectomics of brain disorders. Nat. Rev. Neurosci. 16, 159–172.

Frässle, S., Lomakina, E.I., Kasper, L., Manjaly, Z.M., Leff, A., Pruessmann, K.P., Buhmann, J.M., Stephan, K.E., 2018a. A generative model of whole-brain effective connectivity. Neuroimage 179, 505–529.

Frässle, S., Lomakina, E.I., Razi, A., Friston, K.J., Buhmann, J.M., Stephan, K.E., 2017. Regression DCM for fMRI. Neuroimage 155, 406–421.

Frässle, S., Paulus, F.M., Krach, S., Schweinberger, S.R., Stephan, K.E., Jansen, A., 2016. Mechanisms of hemispheric lateralization: asymmetric interhemispheric recruitment in the face perception network. Neuroimage 124, 977–988.

Frässle, S., Yao, Y., Schobi, D., Aponte, E.A., Heinzle, J., Stephan, K.E., 2018b. In: Generative Models For Clinical Applications in Computational Psychiatry, 9. Wiley, p. e1460 Interdiscip Rev Cogn Sci.

Freeman, L.C., 1977. Set of measures of centrality based on betweenness. Sociometry 40, 35–41.

Friedman, J., Hastie, T., Tibshirani, R., 2008. Sparse inverse covariance estimation with the graphical lasso. Biostatistics 9, 432–441.

Friston, K., Brown, H.R., Siemerkus, J., Stephan, K.E., 2016. The dysconnection hypothesis. Schizophr. Res. 176, 83–94.

Friston, K., Harrison, L., Penny, W., 2003. Dynamic causal modelling. Neuroimage 19, 1273–1302.

Friston, K., Mattout, J., Trujillo-Barreto, N., Ashburner, J., Penny, W., 2007. Variational free energy and the Laplace approximation. Neuroimage 34, 220–234.

Friston, K.J., 1998. The disconnection hypothesis. Schizophr. Res. 30, 115–125.

Friston, K.J., 2009. Modalities, modes, and models in functional neuroimaging. Science 326, 399–403.

Friston, K.J., 2011. Functional and effective connectivity: a review. Brain Connect 1, 13–36.

Friston, K.J., Fletcher, P., Josephs, O., Holmes, A., Rugg, M.D., Turner, R., 1998. Event-related fMRI: characterizing differential responses. Neuroimage 7, 30–40.

Friston, K.J., Mechelli, A., Turner, R., Price, C.J., 2000. Nonlinear responses in fMRI: the Balloon model, Volterra kernels, and other hemodynamics. Neuroimage 12, 466–477.

Froudist-Walsh, S., Browning, P.G.F., Young, J.J., Murphy, K.L., Mars, R.B., Fleysher, L., Croxson, P.L., 2018. Macro-connectomics and microstructure predict dynamic plasticity patterns in the non-human primate brain. Elife 7, e34354.

Gates, K.M., Molenaar, P.C.M., Iyer, S.P., Nigg, J.T., Fair, D.A., 2014. Organizing heterogeneous samples using community detection of GIMME-derived resting state functional networks. Plos One 9, e91322.

Gazzaniga, M.S., 2000. Cerebral specialization and interhemispheric communication: does the corpus callosum enable the human condition? Brain 123 (Pt 7), 1293–1326.

Gilson, M., Deco, G., Friston, K.J., Hagmann, P., Mantini, D., Betti, V., Romani, G.L., Corbetta, M., 2017. Effective connectivity inferred from fMRI transition dynamics during movie viewing points to a balanced reconfiguration of cortical interactions. Neuroimage. 180, 534–546.

Glasser, M.F., Coalson, T.S., Robinson, E.C., Hacker, C.D., Harwell, J., Yacoub, E., Ugurbil, K., Andersson, J., Beckmann, C.F., Jenkinson, M., Smith, S.M., Van Essen, D.C., 2016. A multi-modal parcellation of human cerebral cortex. Nature 536, 171–178.

Goebel, R., Roebroeck, A., Kim, D.S., Formisano, E., 2003. Investigating directed cortical interactions in time-resolved fMRI data using vector autoregressive modeling and Granger causality mapping. Magn. Reson. Imaging 21, 1251–1261.

Goldberg, G., 1985. Supplementary Motor Area Structure and Function - Review and Hypotheses. Behav. Brain Sci. 8, 567–588.

Grefkes, C., Eickhoff, S., Nowak, D., Dafotakis, M., Fink, G., 2008. Dynamic intra- and interhemispheric interactions during unilateral and bilateral hand movements assessed with fMRI and DCM. Neuroimage 41, 1382–1394.

Hagmann, P., 2005. From Diffusion MRI to Brain Connectomics. EPFL, Lausanne.

Halsband, U., Passingham, R., 1982. The role of premotor and parietal cortex in the direction of action. Brain Res. 240, 368–372.

Hoult, D.I., Lauterbur, P.C., 1979. Sensitivity of the zeugmatographic experiment involving human samples. J. Magn. Reson. 34, 425–433.

Ji, J.L., Spronk, M., Kulkarni, K., Repovs, G., Anticevic, A., Cole, M.W., 2019. Mapping the human brain's cortical-subcortical functional network organization. Neuroimage 185, 35–57.

Jirsa, V.K., Proix, T., Perdikis, D., Woodman, M.M., Wang, H., Gonzalez-Martinez, J., Bernard, C., Bénar, C., Guye, M., Chauvel, P., Bartolomei, F., 2016. The Virtual Epileptic Patient: individualized whole-brain models of epilepsy spread. Neuroimage. 145, 377–388.

Jirsa, V.K., Sporns, O., Breakspear, M., Deco, G., McIntosh, A.R., 2010. Towards the virtual brain: network modeling of the intact and the damaged brain. Arch. Ital. Biol. 148, 189–205.

Karahanoglu, F.I., Van De Ville, D., 2017. Dynamics of large-scale fMRI networks: deconstruct brain activity to build better models of brain function. Curr. Opin. Biomed. Eng. 3, 28–36.

Kasper, L., Bollmann, S., Diaconescu, A.O., Hutton, C., Heinzle, J., Iglesias, S., Hauser, T.U., Sebold, M., Manjaly, Z.M., Pruessmann, K.P., Stephan, K.E., 2017. The PhysIO toolbox for modeling physiological noise in fMRI data. J. Neurosci. Methods 276, 56–72.

Kawashima, R., Roland, P.E., O'Sullivan, B.T., 1995. Functional anatomy of reaching and visuomotor learning: a positron emission tomography study. Cereb. Cortex 5, 111–122.

Kim, S.G., Ashe, J., Hendrich, K., Ellermann, J.M., Merkle, H., Ugurbil, K., Georgopoulos, A.P., 1993. Functional magnetic resonance imaging of motor cortex: hemispheric asymmetry and handedness. Science 261, 615–617.

Kötter, R., Stephan, K.E., 1997. Useless or helpful? The "limbic system" concept. Rev Neurosci 8, 139–145.

Kötter, R., Stephan, K., 2003. Network participation indices: characterizing componet roles for information processing in neural networks. Neural Netw. 16, 1261–1275.

Kraskov, A., Prabhu, G., Quallo, M.M., Lemon, R.N., Brochier, T., 2011. Ventral premotor-motor cortex interactions in the macaque monkey during grasp: response of single neurons to intracortical microstimulation. J. Neurosci. 31, 8812–8821.

Ledberg, A., Bressler, S.L., Ding, M., Coppola, R., Nakamura, R., 2007. Large-scale visuomotor integration in the cerebral cortex. Cereb. Cortex 17, 44–62.

Levy, J., 1969. Possible basis for the evolution of lateral specialization of the human brain. Nature 224, 614–615.

Lin, F.H., Tsai, K.W., Chu, Y.H., Witzel, T., Nummenmaa, A., Raij, T., Ahveninen, J., Kuo, W.J., Belliveau, J.W., 2012. Ultrafast inverse imaging techniques for fMRI. Neuroimage 62, 699–705.

Menon, V., 2011. Large-scale brain networks and psychopathology: a unifying triple network model. Trends Cogn. Sci. 15, 483–506.

Mesulam, M.M., 1981. A cortical network for directed attention and unilateral neglect. Ann. Neurol. 10, 309–325.

Mumford, J.A., Ramsey, J.D., 2014. Bayesian networks for fMRI: a primer. Neuroimage 86, 573–582.

Park, H.J., Friston, K., 2013. Structural and functional brain networks: from connections to cognition. Science 342, 1238411.

Passingham, R.E., Stephan, K.E., Kotter, R., 2002. The anatomical basis of functional localization in the cortex. Nat. Rev. Neurosci. 3, 606–616.

Penfield, W., Boldrey, E., 1937. Somatic motor and sensory representation in the cerebral cortex of man as studied by electrical stimulation. Brain 60, 389–443.

Poldrack, R.A., Farah, M.J., 2015. Progress and challenges in probing the human brain. Nature 526, 371–379.

Prando, G., Zorzi, M., Bertoldo, A., Corbetta, M., Zorzi, M., Chiuso, A., 2019. Sparse DCM for whole-brain effective connectivity from resting-state fMRI data. Neuroimage 208, 116367.

Ramsey, J., Glymour, M., Sanchez-Romero, R., Glymour, C., 2017. A million variables and more: the Fast Greedy Equivalence Search algorithm for learning high-dimensional graphical causal models, with an application to functional magnetic resonance images. Int. J. Data Sci. Anal. 3, 121–129.

Ramsey, J.D., Hanson, S.J., Hanson, C., Halchenko, Y.O., Poldrack, R.A., Glymour, C., 2010. Six problems for causal inference from fMRI. Neuroimage 49, 1545–1558.

Rao, S.M., Binder, J.R., Bandettini, P.A., Hammeke, T.A., Yetkin, F.Z., Jesmanowicz, A., Lisk, L.M., Morris, G.L., Mueller, W.M., Estkowski, L.D., et al., 1993. Functional magnetic resonance imaging of complex human movements. Neurology 43, 2311–2318.

Razi, A., Seghier, M.L., Zhou, Y., McColgan, P., Zeidman, P., Park, H.J., Sporns, O., Rees, G., Friston, K.J., 2017. Large-scale DCMs for resting-state fMRI. Netw. Neuroscie. 1, 222–241.

Rizzolatti, G., Luppino, G., 2001. The cortical motor system. Neuron 31, 889–901.

Roebroeck, A., Formisano, E., Goebel, R., 2005. Mapping directed influence over the brain using Granger causality and fMRI. Neuroimage 25, 230–242.

Roland, P.E., Zilles, K., 1996. Functions and structures of the motor cortices in humans. Curr. Opin. Neurobiol. 6, 773–781.

Rubinov, M., Sporns, O., 2010. Complex network measures of brain connectivity: uses and interpretations. Neuroimage 52, 1059–1069.

Sanchez-Romero, R., Ramsey, J.D., Zhang, K., Glymour, M.R.K., Huang, B., Glymour, C., 2018. Causal Discovery of Feedback Networks with Functional Magnetic Resonance Imaging. doi:10.1101/245936.

Sanchez-Romero, R., Ramsey, J.D., Zhang, K., Glymour, M.R.K., Huang, B., Glymour, C., 2019. Estimating feedforward and feedback effective connections from fMRI time series: assessments of statistical methods. Netw. Neurosci. 3, 274–306.

Schaefer, P.W., Grant, P.E., Gonzalez, R.G., 2000. Diffusion-weighted MR imaging of the brain. Radiology 217, 331–345.

Seth, A.K., 2010. A MATLAB toolbox for Granger causal connectivity analysis. J. Neurosci. Methods 186, 262–273.

Seth, A.K., Chorley, P., Barnett, L.C., 2013. Granger causality analysis of fMRI BOLD signals is invariant to hemodynamic convolution but not downsampling. Neuroimage 65, 540–555.

Singh, M.F., Braver, T.S., Cole, M.W., Ching, S., 2020. Estimation and validation of individualized dynamic brain models with resting state fMRI. Neuroimage, 117046.
Smith, S.M., Miller, K.L., Salimi-Khorshidi, G., Webster, M., Beckmann, C.F., Nichols, T.E., Ramsey, J.D., Woolrich, M.W., 2011. Network modelling methods for FMRI. Neuroimage 54, 875–891.
Smith, S.M., Nichols, T.E., Vidaurre, D., Winkler, A.M., Behrens, T.E., Glasser, M.F., Ugurbil, K., Barch, D.M., Van Essen, D.C., Miller, K.L., 2015. A positive-negative mode of population covariation links brain connectivity, demographics and behavior. Nat. Neurosci. 18, 1565–1567.
Sokolov, A.A., Zeidman, P., Erb, M., Ryvlin, P., Pavlova, M.A., Friston, K.J., 2019. Linking structural and effective brain connectivity: structurally informed Parametric Empirical Bayes (si-PEB). Brain Struct. Funct. 224, 205–217.
Sporns, O., Tononi, G., Kotter, R., 2005. The human connectome: a structural description of the human brain. PLoS Comput. Biol. 1, e42.
Stam, C.J., 2014. Modern network science of neurological disorders. Nat. Rev. Neurosci. 15, 683–695.
Stephan, K., Baldeweg, T., Friston, K., 2006. Synaptic plasticity and dysconnection in schizophrenia. Biol. Psychiatry 59, 929–939.
Stephan, K., Friston, K., Frith, C., 2009a. Dysconnection in Schizophrenia: from abnormal synaptic plasticity to failures of self-monitoring. Schizophr. Bull. 35, 509–527.
Stephan, K., Marshall, J., Penny, W., Friston, K., Fink, G., 2007. Interhemispheric integration of visual processing during task-driven lateralization. J. Neurosci. 27, 3512–3522.
Stephan, K., Penny, W., Daunizeau, J., Moran, R., Friston, K., 2009b. Bayesian model selection for group studies. Neuroimage 46, 1004–1017.
Stephan, K.E., Iglesias, S., Heinzle, J., Diaconescu, A.O., 2015. Translational perspectives for computational neuroimaging. Neuron 87, 716–732.
Stephan, K.E., Tittgemeyer, M., Knösche, T.R., Moran, R.J., Friston, K.J., 2009c. Tractography-based priors for dynamic causal models. Neuroimage 47, 1628–1638.
Takemura, S., Bharioke, A., Lu, Z.Y., Nern, A., Vitaladevuni, S., Rivlin, P.K., Katz, W.T., Olbris, D.J., Plaza, S.M., Winston, P., Zhao, T., Horne, J.A., Fetter, R.D., Takemura, S., Blazek, K., Chang, L.A., Ogundeyi, O., Saunders, M.A., Shapiro, V., Sigmund, C., Rubin, G.M., Scheffer, L.K., Meinertzhagen, I.A., Chklovskii, D.B., 2013. A visual motion detection circuit suggested by Drosophila connectomics. Nature 500, 175 –+.
Tavor, I., Jones, O.P., Mars, R.B., Smith, S.M., Behrens, T.E., Jbabdi, S., 2016. Task-free MRI predicts individual differences in brain activity during task performance. Science 352, 216–220.
Tzourio-Mazoyer, N., Landeau, B., Papathanassiou, D., Crivello, F., Etard, O., Delcroix, N., Mazoyer, B., Joliot, M., 2002. Automated anatomical labeling of activations in SPM using a macroscopic anatomical parcellation of the MNI MRI single-subject brain. Neuroimage 15, 273–289.
Valdes-Sosa, P.A., Roebroeck, A., Daunizeau, J., Friston, K., 2011. Effective connectivity: influence, causality and biophysical modeling. Neuroimage 58, 339–361.
Van Essen, D.C., Smith, S.M., Barch, D.M., Behrens, T.E.J., Yacoub, E., Ugurbil, K., Consortium, W.-M.H., 2013. The WU-Minn human connectome project: an overview. Neuroimage 80, 62–79.
Vaughan, J.T., Garwood, M., Collins, C.M., Liu, W., DelaBarre, L., Adriany, G., Andersen, P., Merkle, H., Goebel, R., Smith, M.B., Ugurbil, K., 2001. 7T vs. 4T: RF power, homogeneity, and signal-to-noise comparison in head images. Magn. Reson. Med. 46, 24–30.
Wang, P., Kong, R., Kong, X.L., Liegeois, R., Orban, C., Deco, G., van den Heuvel, M.P., Yeo, B.T.T., 2019. Inversion of a large-scale circuit model reveals a cortical hierarchy in the dynamic resting human brain. Sci. Adv. 5. doi:10.1126/sciadv.aat7854.
Wenderoth, N., Debaere, F., Sunaert, S., Swinnen, S.P., 2005. The role of anterior cingulate cortex and precuneus in the coordination of motor behaviour. Eur. J. Neurosci. 22, 235–246.
White, J.G., Southgate, E., Thomson, J.N., Brenner, S., 1986. The structure of the nervous-system of the Nematode Caenorhabditis-Elegans. Philos. Trans. Royal Soc. B-Biol. Sci. 314, 1–340.
Whittaker, J., 1990. Graphical Models in Applied Multivariate Statistics. Wiley, Chichester England; New York.
Witt, S.T., Laird, A.R., Meyerand, M.E., 2008. Functional neuroimaging correlates of finger-tapping task variations: an ALE meta-analysis. Neuroimage 42, 343–356.
Xia, M., Wang, J., He, Y., 2013. BrainNet Viewer: a network visualization tool for human brain connectomics. PLoS One 8, e68910.
Xu, J., Moeller, S., Auerbach, E.J., Strupp, J., Smith, S.M., Feinberg, D.A., Yacoub, E., Uğurbil, K., 2013. Evaluation of slice accelerations using multiband echo planar imaging at 3 T. Neuroimage 83, 991–1001.
Xu, N., Spreng, R.N., Doerschuk, P.C., 2017. Initial validation for the estimation of resting-state fMRI effective connectivity by a generalization of the correlation approach. Front. Neurosci. 11, 271.
Zeki, S., Shipp, S., 1988. The functional logic of cortical connections. Nature 335, 311–317.